The quest for contrast in digital images of micro-nano structured polymer blends before and after CO2 foaming: General interest of directional diffusive filtering for edge enhancement

Yannick Anguy, Margaux Haurat, Michel Dumon

The quest for contrast in digital images of micro-nano structured polymer blends before and after CO_2 foaming: General interest of directional diffusive filtering for edge enhancement

Yannick Anguy [1,✉], Margaux Haurat [2] and Michel Dumon [2,✉]

[1] Université de Bordeaux, UMR CNRS 5295 I2M, F-33405, Talence, France.
[2] Université de Bordeaux, UMR CNRS 5629 LCPO, Bordeaux INP, F-33600 Pessac, France.

✉ Contact authors : yannick.anguy@u-bordeaux.fr (Yannick Anguy) and michel.dumon@u-bordeaux.fr (Michel Dumon)

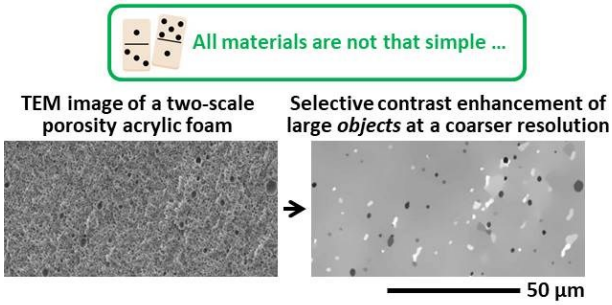

For table of contents use only

Abstract

Multiphase materials composed of several phases with smooth interphases and/or sharp interfaces are ubiquitous in polymer science. This study addresses the challenge to identify and segment automatically the right interfaces and interphases in electronic digital images for a sound analysis of the structuration of materials at the micro-nano scale. The selected strategy is to primarily enhance contrast between phases in digital TEM / SEM images for a straightforward subsequent segmentation of phases i.e., by a simple threshold of the grey level intensity histogram. To do so, a nonlinear transient (time dependent) diffusion process is used. In the diffusive process, the grey level intensity spreads non-uniformly across the image pixels i.e., adaptively to local properties of the image. When computed at a large enough time of the diffusive process, the reconstructed image tends to a piecewise constant solution representing a simplified image at a lower resolution with sharper boundaries, bringing the sought local contrast enhancement. The solution image is shown to facilitate the automatic segmentation step and calculation of representative size distributions. This approach is in particular very suited to the characterization of multimodal samples including different scales of porosity. While this (first of two parts) methodological article is useful to multiphase polymeric materials in general, the methodology was here developed for an in-depth study of acrylic block copolymer nanostructures enabling to monitor micro-nano sized foams produced by one step batch $scCO_2$ green foaming.

Keywords : micro-nano foams; one-step batch CO_2 foaming; acrylic polymers and copolymers; quantitative structural analysis; contrast enhancement; edge enhancement; polymer structured blend materials; electron microscopies.

1. INTRODUCTION

There is a vast literature on the occurrence of multiphase materials composed of several phases with smooth interphases and/or sharp interfaces. Phases, interphases and interfaces are of crucial importance in several domains of polymer science including control of material properties [1] [2] [3], polymerization efficiency [4] [5] [6] or refined characterizations of materials [3] [7] [8] [9] [10].

Smooth interphases and sharp interfaces are more or less difficult to reveal, characterize and quantify, particularly at the nanometer scale. At this scale level, transmission electron microscopy (TEM) or scanning electron microscopy (SEM) are often used to observe and characterize multiphase materials [1] [2] [4] [5] [7] [8] [9]. The correct characterization of the materials requires typically **1)** use of a suitable contrasting method or a contrasting aid [6] e.g., sputtering for SEM or staining for TEM, **2)** imaging in proper conditions (temperature, pressure, electron flow) and **3)** establishing robust methods or refined image treatments [11] [12] [13] [14] [15] [16] [17] [18] [19], in other words *a good image analysis*, leading to a representative quantification of the different phases.

This methodological contribution addresses the ubiquitous challenge to identify and segment the right interfaces and interphases for a sound analysis of the structuration of organic multiphase materials at the micro and nanoscale. With regard to the three requirements recalled above for a correct characterization of materials, the proposed methodology may be positioned as follows: it fits in requirement 1 i.e., reaching a suitable level of contrast, while remaining within the bosom of image analysis (requirement 3). In digital images, the level of contrast can be enhanced in different ways, always complementary. A staining procedure is for example often used prior to image formation in TEM imaging. Combining different approaches to contrast enhancement is always beneficial. For instance, contrast can be further heightened by technical solutions such as energy filtered TEM or scanning transmission electronic microscopy coupled to energy dispersive spectroscopy. Yet, such facilities are not always readily available or accessible. The solution proposed in this work is to further augment contrast in images using a directional nonlinear diffusive equation whereby the local grey level intensity spreads across the pixels of the digital image. It leads to *a kind of image virtual reconstruction* where object boundaries are adaptably and selectively enhanced (contrasted) for a simpler subsequent segmentation of phases.

The methodological work presented here was initiated and motivated for an in-depth study of micro-nano sized polymeric foams and the relations between the foaming process and accurate morphological characterizations carried out at different scales [20]. While the selected method may be useful for most multiphase materials and over a broad range of scales, the methodology is illustrated with the example of a multiphase organic material in two different states: solid state polymer blends (foam precursors with isolated nanodomains) and resulting $scCO_2$ blown foams. The organic material is composed of only acrylic polymers: an homopolymer matrix i.e., PMMA, poly(methyl methacrylate), a dispersed triblock copolymer called MAM, poly (methyl methacrylate-co-butylacrylate-co-methyl methacrylate), and voids after foaming. Due to chemical similarity and covalent bonds between blocks, MAM separates at the nano-level as micellar-like objects in the PMMA matrix. Those micellar nanostructures are deemed to act as CO_2 enhanced reservoirs compared to PMMA matrix. They behave as efficient nucleants when CO_2 foaming is triggered. Foaming is obtained in one-step solid-state (non-flowing) batch i.e., a discontinuous physical process whereby the block copolymer acts as a foaming aid helping to regulate pore size distribution [20] [21] [22] [23] [24] [25] [26]. The PMMA/MAM system may be viewed as a *model system* based on amorphous, non additivated and hence almost pure PMMA. PMMA shows very good optical properties as well as an excellent resistance to ageing, which makes it very suitable for headlights, packaging boxes, lenses or windows manufacturing. Addition of a small amount of low cost MAM (containing an elastomer component) to the brittle PMMA makes it more ductile, thereby improving its mechanical properties, while preserving its optical properties (transparency and refractive index). This system has been widely investigated in the literature, which makes it a good candidate to appraise the benefits of the proposed method of image optimization.

In solid-state batch one-step $scCO_2$ foaming, the structuration of the final foam depends on the material formulation (e.g., BCP content and size) and on the foaming conditions. For the latter, mention the saturation temperature T_{sat}, the saturation pressure P_{sat} and the average pressure drop rate, which shall all be optimized for each blowing agent – material – process combination. The final porous structure is also strongly influenced by the interplay of the kinetics of several of the intervening physical variables. Mention the respective evolution of the time-dependent material effective temperature $T_{ef}(t)$, the rise of the effective glass transition temperature of the plasticized system $T_{g,ef}(t)$ and the instantaneous drop of the pressure $\frac{dP(t)}{dt}$, which differs from the average pressure drop release value $\frac{\Delta P}{\Delta t} = \frac{P_{sat}-P_{ambient}}{\Delta t}$ (where Δt is the time to return to ambient pressure upon pressure release) [23].

Understanding the separate impact of those multiple factors on foam structuration can be greatly facilitated when **(1)** the BCP size distribution of the unfoamed material and **(2)** the cell size distribution of the foam are quantified (the latter being always influenced by the former). Availability of those statistical distributions i.e., the quantified input and output of the foaming process is one of the keys towards understanding and optimizing the foaming process. Along the same lines, in a study of the impact of component rheology and compatibility upon the final morphology of polyolefin blends, Kock et al. have stressed that a key factor in this type of analysis is availability of the particle size distribution from an independent analysis, like image analysis on electron micrographs [27]. Yet, these authors also note that there have been many problems inherent in quantification of phase separation morphology. Similarly, Miyata et al. [28] and Xu et al. [29] have reported that despite its importance, there was rarely a simple and useful method for the quantitative assessment of morphology. Whichever method is used to quantify the phase-separated domains morphology e.g., the cross-correlation analysis [30], the fractal approach [28] [29] or the local Crofton method (this study), its accuracy primarily depends upon the exactness of the labeled phase domains (segmentation) upstream in the image analysis chain. There is no single route to address the recurrent segmentation bottleneck. With the ongoing development of machine learning approaches, the segmentation issue may be advantageously transformed to a pixel classification issue [31] [32]. Yet, the user interaction is still required to train the classifier. Another road is taken in the present study. Segmentation is mainly facilitated by preliminarily enhancing the original contrast in electronic

micrographs relying on the so-called scale-space filtering formalism [33] [34] [35] [36] [37], which is to the best of the authors' knowledge innovatively applied to polymer science.

Thus, the primary aim of this work is the analysis of electronic images of the structuration of multiphase polymeric micro-nano structured materials before and after $scCO_2$ foaming. The selected approach builds on a multiscale (multiresolution) description of electronic images, hereafter denoted by $u(\mathbf{x})$, and mapping the grey level intensity u (the luminance) at any pixel $\mathbf{x} = (x_1, x_2)$. According to this formalism (scale-space filtering), the original image $u(\mathbf{x})$ is embedded in a family of images $u(\mathbf{x}, t)$ at coarser resolutions (larger scale levels of description). This family of images, $u(\mathbf{x}, t)$, is obtained by filtering the original image $u(\mathbf{x})$ over increasing scales whose size is parametrized by the time t of a diffusion process. During the diffusive process, the local grey level intensity u spreads across the image. The increasing time t of the diffusive filter acts as the scale-space parameter.

The underlying justification of this approach is that images have by nature a hierarchical or pyramidal organization composed of a small number of relevant, or more precisely, of *semantic* levels of description [38]. In a pioneer work published in 1990, Perona and Malik [39] showed that there is a natural range of resolutions i.e., intervals of the scale-space parameter t of the diffusive filter, corresponding to each of these semantic levels of description. While moving with time t across the scales of the pyramid by letting diffuse the grey level intensity u, it is therefore expected to find the semantic interval(s) of the scale-space parameter t allowing to better perceive the interphases and interfaces of interest.

The approach per se is not new. It has been widely used in the field of image restoration and denoising. Yet, the use made of this approach here and the *quest* which is pursued are not the usual ones. Application of this approach to polymer science is also new. The approach is used as a method for *virtually reconstructing* interfaces and interphases, thereby providing *new image reconstructions*. Our quest is local contrast enhancement of the only objects of interest, in order to facilitate their subsequent segmentation e.g., by a simple thresholding of the grey level intensity histogram.

2. EXPERIMENTAL

2.1 Materials

Neat PMMA poly(methyl methacrylate) commercialized as *V825T 101 Clear grade* was initially supplied by Arkema Company (Lacq, France) in the form of pellets. It is now commercialized by Trinseo. Neat MAM triblock copolymer pellets (poly(methyl methacrylate)-co-poly(butyl acrylate)-co-poly(methyl methacrylate)) were also supplied by Arkema Company. This triblock copolymer (commercial name *Nanostrength M53*) has a 54 wt% content of the soft block, poly (butyl acrylate) (PBA). The characteristics of these materials are well documented in the literature [24] [40] [41].

2.2 Unfoamed solid blends production

PMMA/MAM blends of different MAM content were compounded at CANOE (Pau, France) using a Labtech co-rotative twin-screw extruder, with L/D ratio of 40 and a screw diameter of 26 mm. Before compounding, PMMA and MAM pellets were dried at 80°C for 4 hours. Then, the blends were extruded at a screw speed of 300 rpm with a temperature profile from 250 °C at the extruder inlet to 230 °C in the die. The blends were pelletized using a continuous cutting machine operating at the end of the line.

The PMMA/MAM pellets were dried again at 80°C for 4 hours. Transparent tensile test bars (ISO 180/U $80 \times 10 \times 4$ mm^3) of PMMA/MAM were injected with an ENGEL ES 200-45 HL-V injection-molding device. The acrylic blends were injected at 230 °C at a speed of 300 rpm in a mold heated at 90 °C. All injected bulk bars were perfectly transparent.

2.3 Gas physical foaming experiments

Foaming experiments were performed in a high-pressure vessel provided by TOP Industrie (Vaux-le-Pénil, France) with a capacity of 0.3 L. Foaming was performed using a one-step discontinuous process [40] [42] [43] [44]. Bulk solid samples were introduced in the vessel under 30 MPa of CO_2 pressure for the saturation stage (24h). These transparent samples are the foam precursors. Two different saturation temperatures were used, 40 °C and 60°C. After saturation (in supercritical conditions), pressure was released at an average pressure drop rate of 0.5 MPa/s. Foaming occurred upon depressurization. Samples were taken out of the autoclave as white foamed solids.

2.4 Characterization methods / Basis of the image analysis

2.4.1 Nanostructuration of the solid blends

The structure of the partially miscible PMMA/MAM blend precursors was analyzed by transmission electron microscopy (TEM). Prior to the observation, each material was cut in ultra-thin slices (with a thickness of approximately 80 nm) using a Leica EM UC7-FC7 ultra microtome. Due to the soft behavior of the polymer blend, samples were cut in cryogenic conditions at -75°C. Slices were then collected and laid down onto 200 mesh copper grids.

TEM images were collected at the Bordeaux Imaging Center (BIC, Bordeaux France) with a Hitachi H7650 electron microscope equipped with a camera SC1000 ORIUS 11Mpx (GATAN). The acceleration voltage was 80 kV. The aperture size of the condenser diaphragm was 200 µm. A lens diaphragm of 90 µm was used.

Recall that the high voltage of a TEM provides typically little contrast between materials such as PMMA and the elastomeric block (PBA) [45].

As a first aid to increase contrast between the PMMA matrix and the dispersed nanostructures, a coloration (staining) of the elastomeric phase was carried out with an aqueous solution containing 2 wt% of phosphotungstic acid (PTA) and 2 wt%. of benzyl alcohol [22] [46]. The grid was kept in contact with a drop of PTA solution during 10 min at room temperature and then rinsed with water. As a result of this, the nanostructures could be better perceived on TEM micrographs e.g., Figure 1. The micellar objects appear essentially as dispersed nanosized convex core-shell particles with a brighter PMMA core surrounded by a darker PBA crown preferentially colored by PTA [22] [23] [47]. Such (apparent) two-layer micellar objects would give hints for the inner structure. Two hypotheses can be given:

- In the micellar objects, MAM molecules are U-shaped; the PBA central block is located *at the heart* of the U whose two parallel branches are made of PMMA molecules. The PMMA core entrapped in the micelle arises most probably from the PMMA matrix.
- Or, in the micellar objects, MAM molecules show linear I-shaped chains.

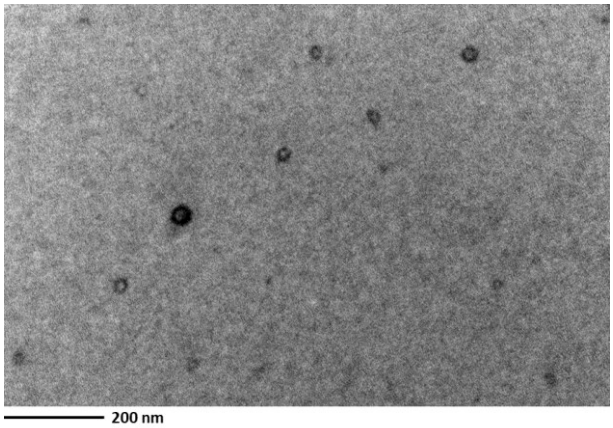

Figure 1. High resolution (magnification 150 kX) TEM micrograph showing the core-shell-like structure of MAM tri-block copolymer in a 99.75/0.25 wt% PMMA/MAM solid blend after staining.

In Figure 1, the micellar nanostructures are contrasted by PTA with a strength that varies locally. Some micellar objects contrasts better with the background matrix than some other micelles. The common belief that PTA should color uniformly the only PBA component of the nanostructures may be too simple. Besides, several authors claim even otherwise [48] [49]. Contrast disparity among nanostructures may arise from the fact that the selective staining power of PTA depends on several properties that may vary locally. Such properties include solubility, hydrophobicity, swelling capability of PBA by benzyl alcohol and softness[1], to which the influence of the surrounding phases may be added. Moreover, PBA may not occur in its micellar-like form only. Part of MAM may remain dissolved (as miscible chains in PMMA chains) and this may locally weaken the contrast aid brought by staining.

In addition, as PTA staining is made by liquid diffusion, coloration is essentially a surface selective physical process. Therefore, the achieved contrast is not homogeneous in the preparation thickness.

Electronic micrographs typified by inhomogeneous contrast between objects (foreground) and the background have been widely analyzed by hybrid methods combining both automatic and manual image analysis procedures. For example, Pinto et al. [50] developed under FIJI/ImageJ [51] a user interactive image analysis combining standard filters for image optimization / binarization followed by a user interactive selection and validation of well binarized objects.

[1] The preferential swelling of a soft phase with alkyl groups in presence of benzyl alcohol surely promotes the selective staining of PBA.

Such user-interactive approach produced sufficient results to show the relevance of BCP addition for forcing nucleation [23] [47]. Object sizes have also been measured using the user-interactive Piximeter software [52].

Despite their value in polymer science, the widespread semiautomatic image analysis approaches still include part of the inconvenience of manual methods e.g., a somewhat limited number of measured objects, any subjectivity in sampling (with the concomitant risk to miss or overlook certain characteristics such as multimodality) and/or tediousness. With respect to such inconveniences, Kock et al. report how their image analysis, based on the ImageJ software for determining the average particle sizes in binary polyolefin blends, was so laborious that only a limited number of blends could be practically used for this determination [27]. Mae et al. analyzed the size of SEBS particles dispersed in a PP matrix using the commercial image analysis software Azo-kun, Asahi Kasei Engineering, Japan [53]. The diameter of each rubber particle was collected manually because the particles could not be correctly segmented by a simple threshold.

Therefore, this work is a further step towards determining in a fully automatic (and simple) manner the objects statistical size distribution (the proposed solution could be ultimately fitted in the above approaches). The proposed approach allows to process very rapidly thousands and even tens of thousands of objects.

Because inhomogeneous contrast is the main source of error in the automatic binarization step [50], it is highly advisable to first further increase the contrast ratio permitted by staining. Similarly, in their analysis of images of PP/EOC elastomer polymer blends using the software ImageJ, Svoboda et al. have reported that at first it is required to increase the contrast between phases in the original stained (RuO_4 vapor) TEM images [54]. In the same way, Poelt et al. characterized the size of the modifier particles in SEM pictures of PP matrices blended with ethylene–propylene copolymer rubber using the Noran Voyager image-analysis system [55]. They insist on that the higher the contrast in the original image, the simpler image processing is, reducing all the more its influence upon the calculated particle size distribution.

In view of the above, the present study, focused on substantially enhancing contrast in the original (stained) images, aims at breaking down the image analysis/segmentation *lock* through a sound, simple and automatic image analysis approach, which has never been applied to polymer science.

2.4.2 Cellular structure

The cellular structure of the samples was imaged at Laboratory I2M using an environmental scanning electron microscope (a ThermoFisher Quanta 250 FEG ESEM). For the observation, samples were fractured (perpendicularly to the direction of barrels injection) after cooling in liquid nitrogen. They were next coated with a gold layer of a few nanometers thick using a sputter coater. The cellular structure of the porous materials foamed from the solid blend precursor imaged in Figure 1 is illustrated in Figure 2. This image (Figure 2) was formed by collecting the secondary electron emission. In this situation, the contrast is said topographical and is made of three contributions: the inclination contrast, the shading contrast and the ridge contrast. Both shading and ridge contrasts promote darker foam cells than the polymeric background solid lattice. Yet, dependence of the secondary emission upon the incident angle of the primary electron beam (inclination contrast) may work locally the other way around, depending on the local geometry of the sample. So, it is here again recommended to further increase contrast before performing a correct fully automatic binarization.

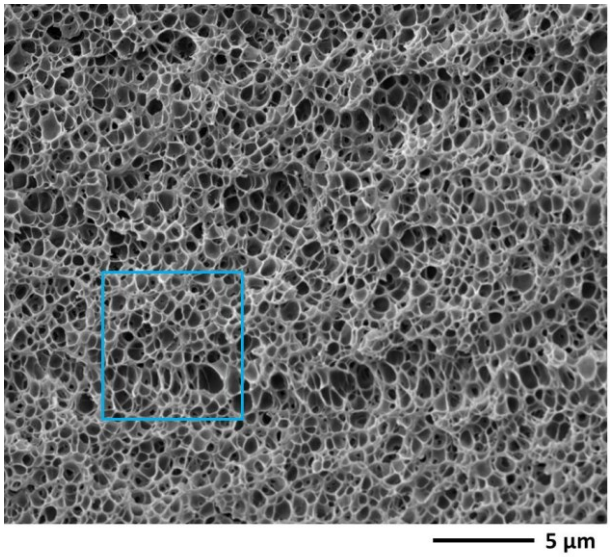

Figure 2. SEM micrograph illustrating the cellular structure of a foam produced from 99.75/0.25 wt% PMMA/MAM blend (Figure 1) at a CO_2 pressure of 30 MPa and at 60°C for the saturation stage and using a pressure drop rate of 0.5 MPa/s (the right blue box is used in Figure 11).

2.4.3 Basis of the image analysis

2.4.3.1 Edge-enhancement by nonlinear filtering upstream of the binarization step

~~A~~ multiscale (or multiresolution) description of electronic images of type Figure 1 and Figure 2 is adopted to further increase contrast (recall that thereafter, images are denoted by $u(\mathbf{x})$, where u is the grey level intensity at every pixel $\mathbf{x} = (x_1, x_2)$). More precisely, the *scale-space filtering* formalism [33] is adopted. In this formalism, the original image $u(\mathbf{x})$ is embedded in a family of images $u(\mathbf{x}, t)$ at coarser resolutions (larger scale levels of description) obtained by filtering $u(\mathbf{x})$ over increasing scales whose size is parametrized by the increasing time t of a diffusion equation.

Use of a diffusion equation in a multiresolution framework originally arose from use of Gaussian filters of variance σ^2. Indeed, the solution $u(\mathbf{x}, t)$ at time $t = \frac{1}{2}\sigma^2$ of the linear diffusion equation[2] given in Eq. 1 along with reflective conditions at the image boundary $\partial\Omega$ (Eq. 2) is the convolution of the original image $u(\mathbf{x})$ by a Gaussian kernel of variance $\sigma^2 = 2t$ (Eq. 3) [34] [56] [57].

$$\partial_t u_{(\mathbf{x},t)} = \nabla.\left(\boldsymbol{\nabla} u_{(\mathbf{x},t)}\right) \text{ on } \Omega, \text{ a bounded domain} \subseteq \mathbb{R}^2 \qquad \text{Eq. 1}$$

$$\partial_{\mathbf{n}} u_{(\mathbf{x},t)} = 0 \text{ on } \partial\Omega \qquad \text{Eq. 2}$$

$$u_{(\mathbf{x},t)} = u_{(\mathbf{x})} * \frac{1}{4\pi t} e^{-\frac{|\mathbf{x}|^2}{4t}} \qquad \text{Eq. 3}$$

In these equations, $\nabla.(\,) = \partial_{x_1}(\,) + \partial_{x_2}(\,) = \frac{\partial}{\partial x_1}(\,) + \frac{\partial}{\partial x_2}(\,)$ is the divergence operator, $\boldsymbol{\nabla}(\,) = \left(\partial_{x_1}, \partial_{x_2}\right)$ is the gradient operator, and $\partial_t = \frac{\partial}{\partial t}$ is the time derivative. In the boundary condition given in Eq. 2, $\mathbf{n}$ is the normal to the image boundary The time t or the variance of the Gaussian act as the scale-space parameter. Larger values of t (or σ) correspond to images filtered (smoothed) at coarser resolutions.

Yet, neither linear isotropic diffusion (Eq. 1 and Eq. 2) nor Gaussian convolution (Eq. 3) are able to maintain edges i.e., interphases and/or interfaces across which the magnitude $\|\boldsymbol{\nabla} u\|$ of the gradient of the intensity function u is large. The reason is that these operators are space invariant [38]. As illustrated in Figure 3, contours are rapidly blurred by increasingly diffuse Gaussians parametrized by $t > 0$ with variance σ^2 satisfying $t = \frac{1}{2}\sigma^2$ [37].

[2] or heat conduction equation if an analogy is drawn between the grey level intensity u and the temperature.

What is needed is a partial differential equation diffusing in a non-uniform manner in order to control the smoothing performed by the low pass filter illustrated in Figure 3. The approach should be based on the local properties of the image in order to control locally the strength of blurring. In this sense, Perona and Malik [39] [58] and Perona et al. [59] proposed in pioneer contributions the nonlinear directional (anisotropic) solution represented by Eq. 4 and Eq. 5 as an efficient alternative to Eq. 1.

$$\partial_t u_{(\mathbf{x},t)} = \nabla.\left(\mathrm{c}(\|\nabla \mathrm{u}\|)_{(\mathbf{x},\mathrm{t})} \nabla u_{(\mathbf{x},t)}\right) \text{ on } \Omega \qquad \text{Eq. 4}$$

$$c(\|\nabla u\|)_{(\mathbf{x},t)} = \frac{1}{1+\frac{\|\nabla u\|^2}{\kappa^2}} \qquad \text{Eq. 5}$$

In these equations, the diffusivity function c is a positive, smooth and non-increasing function of the magnitude $\|\nabla u\|_{(\mathbf{x},t)}$ of the gradient of the local grey level intensity u. Here, $\|\nabla u\|_{(\mathbf{x},t)}$ acts as an estimate of the localization of the boundaries at scale t.

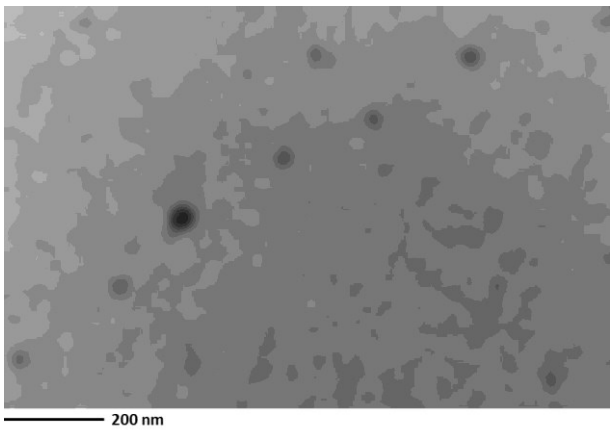

Figure 3. High resolution TEM micrograph of a 99.75/0.25 wt% PMMA/MAM dense blend (Figure 1) after applying the low pass filter described by Eq. 1 and Eq. 2, or Eq. 3. Gaussian blurring (Eq. 3) or isotropic linear diffusion (Eq. 1 and Eq. 2) do not respect the boundaries of the objects. Boundaries are dissipated with increasing time t, when moving towards the higher levels or scales of the pyramidal image.

Let us first make clearer the directional nature of the process. Indeed, this directional nature is going to prove to be the key for strengthening locally contrast. Start by rewriting Eq. 4 in the form of Eq. 6 [60] [61], which also allows to make the link between isotropic (non-directional) linear diffusion (Eq. 1) and anisotropic (directional) nonlinear diffusion (Eq. 4).

$$\partial_t u = c(\|\nabla u\|)\nabla.(\nabla u) + \frac{c'(\|\nabla u\|)}{\|\nabla u\|}(\nabla u)^{\boldsymbol{t}}.\mathbf{H}.\nabla u \qquad \text{Eq. 6}$$

Where $\mathbf{H}$ is the Hessian matrix of u, $(\,)^t$ is the transpose vector and c' is the derivative of c with respect to $\|\nabla u\|$.

From Eq. 6, it is seen that when the diffusion function c is constant, the equation reduces to Eq. 1. In the form of Eq. 6, the nonlinear process may be interpreted as a locally constant isotropic diffusion process combined with a direction-dependent transport term (the second term in the right hand side of Eq. 6) [61].

The anisotropic nature of the process becomes obvious when rewriting Eq. 6 in the form of Eq. 7 i.e., as the sum of the second derivatives of the intensity u in two orthogonal directions. These directional second derivatives are noted $u_{\boldsymbol{\eta\eta}}$ and $u_{\boldsymbol{\xi\xi}}$ in Eq. 7. The first direction has a unit vector $\boldsymbol{\eta} = \frac{\nabla u}{\|\nabla u\|}$ along the gradient of the local grey level intensity u. In other words, $\boldsymbol{\eta}$ is oriented normal to the isolines of the intensity u. The unit vector in the orthogonal direction is denoted by $\boldsymbol{\xi}$ and is normal to the gradient of u. This is to say, $\boldsymbol{\xi}$ is parallel to the isolines of u [60] [62]. In Eq. 7, the second derivatives are weighted by different diffusion coefficients in the two orthogonal directions (represented graphically in Figure 4), which demonstrates the anisotropic nature of the process.

$$\begin{cases} \partial_t u = c(\|\nabla u\|)\, u_{\xi\xi} + \ b(\|\nabla u\|)\, u_{\eta\eta} \\ b = c + \|\nabla u\| c' \end{cases} \qquad \text{Eq. 7}$$

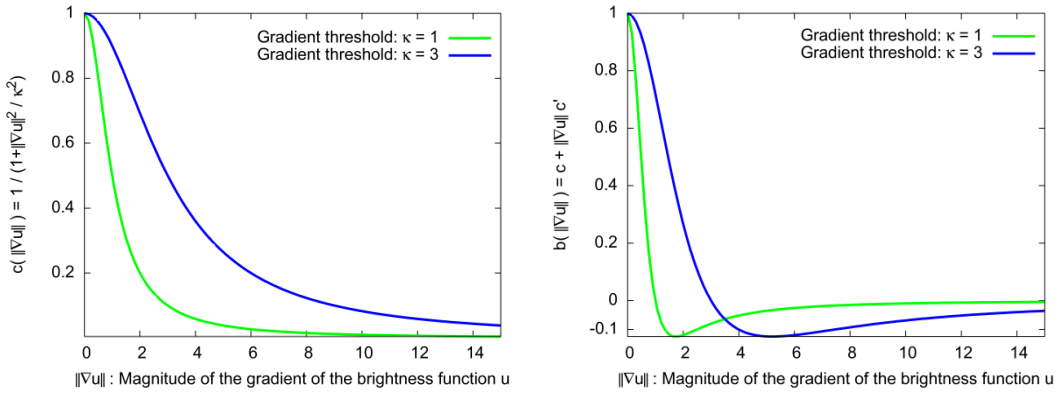

A) **B)**

Figure 4. Graphical representation of the directional coefficients weighting the diffusion process in Eq. 7 when using the diffusion function given in Eq. 5. **A)** Weighting coefficient $c(\|\nabla u\|) = \frac{1}{1+\frac{\|\nabla u\|^2}{\kappa^2}}$ tangential to the level curves of the grey level intensity u. **B)** Weighting coefficient $b(\|\nabla u\|) = c + \|\nabla u\| c' = \frac{\kappa^2(\kappa^2 - \|\nabla u\|^2)}{(\kappa^2 + \|\nabla u\|^2)^2}$ normal to the isolines of u (Eq. 7).

Ideally, the nonlinear diffusion process represented by Eq. 4, Eq. 6 and/or Eq. 7 should be conditional. In flat regions i.e., near pixels $\mathbf{x}$ where $\|\nabla u\|_{(\mathbf{x},t)}$ is small, and therefore, where there is no edge, the diffusion should be high and isotropic (smoothing should be strong) and should act as a low pass filter as does Eq. 1. This is indeed the case, since the weighting diffusion coefficients in Eq. 7 satisfy Eq. 8 (see also Figure 4). Therefore, one is actually left with the desired isotropic linear diffusion in flat regions. Near pixels $\mathbf{x}$ where $\|\nabla u\|_{(\mathbf{x},t)}$ is large i.e., near boundaries or edges**,** the diffusion should be vanishingly small in order to preserve contrast and boundaries. This is also the case since the weighting coefficients in Eq. 7 satisfy Eq. 9 (see also Figure 4). Thus the nonlinear process preserves regions boundaries because diffusion is adaptive to image data (namely $\|\nabla u\|_{(\mathbf{x},t)}$, which acts as an estimate of the localization of boundaries at scale t).

$$\lim_{\|\nabla u\| \to 0} c = 1, \lim_{\|\nabla u\| \to 0} b = \lim_{\|\nabla u\| \to 0} c + \|\nabla u\| c' = 1 \qquad \text{Eq. 8}$$

$$\lim_{\|\nabla u\| \to \infty} c = 0\,, \lim_{\|\nabla u\| \to \infty} b = \lim_{\|\nabla u\| \to \infty} c + \|\nabla u\| c' = 0 \qquad \text{Eq. 9}$$

The so far qualitative statement of *small* and *high* gradient of the grey level intensity u is specified via the parameter κ in the weighting diffusion coefficients in Eq. 7 (see Figure 4 for a graphical representation). Parameter κ acts as a tunable soft gradient threshold or a contrast parameter. It determines which edge slopes will be preserved and which ones will be dissipated [63] [64]. In Figure 4, one can see that where $\|\nabla u\|_{(\mathbf{x},t)}$ is lower than the threshold gradient κ, the directional weighting diffusion coefficients are high and the region is therefore locally homogenized. Where $\|\nabla u\|_{(\mathbf{x},t)}$ is higher than κ, the directional diffusion coefficients are lower and the region contrast is locally preserved. As κ is decreased, this *bascule* between the two regimes is shifted towards smaller gradients of the intensity function u. This is illustrated in Figure 4 where κ takes two values (1 and 3). Therefore, κ distinguishes regions requiring high or low diffusion. This constant κ can be fixed by hand at some fixed value or using, for example, a noise estimator [65] [66] [67]. More information on this issue is provided below.

Yet, edges or boundaries (contrast) at coarser resolutions (at larger values of the scale-space parameter t) shall be sharpened and not only maintained. Edge contrast enhancement actually follows from the directional coefficient weighting diffusion normal to the isolines of u. As illustrated in Figure 4.B, this directional diffusion coefficient ($b(\|\nabla u\|) = c + \|\nabla u\| c'$) turns negative in the neighborhood of the steepest region of a marked discontinuity (edge) (where $\|\nabla u\|_{(\mathbf{x},t)}$ is higher than κ) [68]. In such a situation, Eq. 7 behaves locally as an inverse diffusion equation normal to step-edges. In other words, diffusion is running backwards and step-edges (edges whose contrast is larger than κ) are steepened [69].

Eq. 4 was discretized by finite differences by means of a cheap and simple explicit numerical scheme [62] [70] as

$$\frac{u_{(\mathbf{x},t+dt)} - u_{(\mathbf{x},t)}}{dt} = \sum_i \frac{1}{dx_i^2}\left(\mathrm{c}_{\left(\mathbf{x}+\frac{dx_i}{2}\mathbf{e_i},\ t\right)} \left(u_{(\mathbf{x}+dx_i\,\mathbf{e_i},\ t)} - u_{(\mathbf{x},\ t)}\right) \cdots \right.$$
$$\left. - \mathrm{c}_{\left(\mathbf{x}-\frac{dx_i}{2}\mathbf{e_i},\ t\right)} \left(u_{(\mathbf{x},\ t)} - u_{(\mathbf{x}-dx_i\,\mathbf{e_i},\ t)}\right) \right) \qquad \text{Eq. 10}$$

where dx_i is the pixel size along the Cartesian direction i of unit vector $\mathbf{e_i}$.

The Supporting Information (Numerical discretization) can be consulted for more information on the numerical discretization method. The above discretized equation is written below in a more compact form where $\delta u_{(\mathbf{x},t)}$ denotes the right hand side of Eq. 10.

$$u_{(\mathbf{x},t+dt)} = u_{(\mathbf{x},t)} + \delta u_{(\mathbf{x},t)} \times dt \qquad \text{Eq. 11}$$

The whole explicit scheme consisted in iterating Eq. 11 whereby the grey level values at $t + dt$ are directly calculated from values at t without solving any system of equations. This explicit iterative scheme is therefore computationally very cheap. Convergence of the iterative algorithm is declared when the residual $\delta u_{(\mathbf{x},t)} \times dt$ in Eq. 11 tends towards a vanishingly small value.

2.4.3.2 Parametrization of the nonlinear filter for edge enhancement

Practically, once numerically discretized (Eq. 10 and Eq. 11), use of this directional adaptive diffusive filter only requires to set four parameters: the time step dt i.e., the duration of each iteration, the time t during which diffusion takes its course, the choice of a diffusion function c e.g., Eq. 5, and the contrast parameter κ entering in the definition of the diffusion function. The four parameters are not independent of each other.

Setting the value of the time step dt is not a difficulty. In 2D with 4-connected neighbors, the stability of the explicit scheme allows a time step dt not exceeding 0.2 [67]. The smaller is dt, the smaller is the difference between two successive images at t and $t + dt$ and the larger is the number of iterations and CPU time to reach time length t (the scale level of size t).

Evaluating the appropriate time length t is also not difficult. Yet, it is more subjective. Recall that images are composed of a small number of semantic scale levels of description. A finite interval of the scale-space parameter t corresponds to each of these semantic levels, including the level of description at which the interfaces or interphases of interest can be better perceived (are *virtually reconstructed)*. Time length t is identified a posteriori by sweeping out the scale-space image $u(\boldsymbol{x}, t)$.

In the authors' experience, the diffusion function provided in Eq. 5 brings the sought local contrast enhancement in most instances. Unless specified otherwise, Eq. 5 was systematically used in this work. Yet, the choice of the diffusion function is not unique and some would argue that this choice shall be guided by the characteristics of the image. In this sense, Eq. 12 provides another diffusion function, also proposed by Perona and Malik [39]. See Figure 5 for its graphical representation.

$$c(\|\boldsymbol{\nabla} u\|)_{(\mathbf{x},t)} = \mathrm{e}^{-\left(\|\boldsymbol{\nabla} u\|/\kappa\right)^2} \qquad \text{Eq. 12}$$

The diffusion function in Eq. 12 shows a steeper evolution with $\|\boldsymbol{\nabla} u\|$ than the function in Eq. 5 at a fixed value of the contrast parameter κ (compare Figure 4 to Figure 5). Thus, blurring is stronger when using Eq. 5. At large values of the scale-space parameter t, the scale-space images produced using Eq. 5 or Eq. 12 will be different; the function in Eq. 5 privileges wide regions over smaller ones, while the function in Eq. 12 privileges high contrast edges over low contrast ones [39].

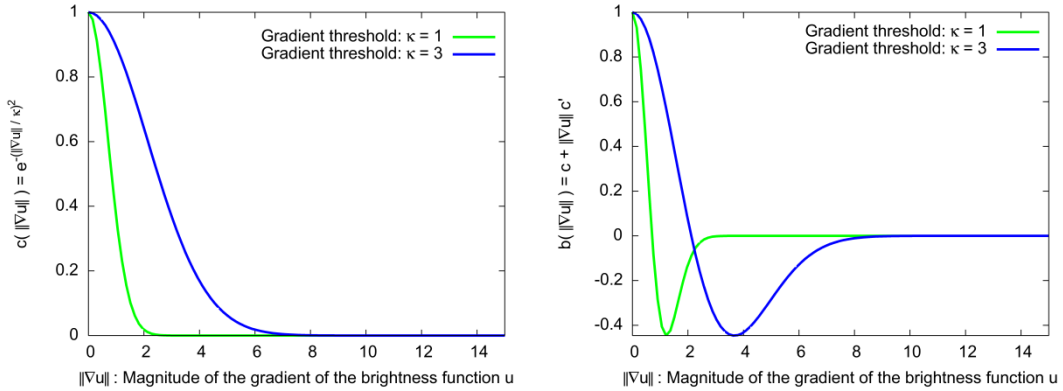

A) **B)**

Figure 5. Graphical representation of the directional coefficients weighting the diffusion process in Eq. 7 when using the diffusion function given in Eq. 12. **A)** Weighting coefficient $c(\|\boldsymbol{\nabla} u\|) = e^{-\left(\|\boldsymbol{\nabla} u\|/\kappa\right)^2}$ tangential to the isolines of the intensity function u. **B)** Weighting coefficient $b(\|\boldsymbol{\nabla} u\|) = c + \|\boldsymbol{\nabla} u\| c' = \left(1 - 2\left(\|\boldsymbol{\nabla} u\|/\kappa\right)^2\right) e^{-\left(\|\boldsymbol{\nabla} u\|/\kappa\right)^2}$ normal to the isolines of u (Eq. 7).

The choice of the threshold parameter κ entering in the diffusion function (Eq. 5 or Eq. 12) is decisive. This threshold parameter acts as an edge-strength threshold. If its value is too high, the diffusion process will oversmooth and lead to a blurred image. If κ is too small, the diffusion process will stop smoothing too early, leading to a filtered solution too close to the original image [71]. The suitable value for κ may be chosen on the basis of the local standard deviation of the image (calculated over a sliding small window of size $m \times m$ pixels). Recall that the local standard deviation of an image may be related to the *noise level* in the image. Gerig et al. estimated noise level as the lowest local standard deviation in the background and in the foreground [66]. Their idea was that a local area showing the smallest grey level dispersion represents a homogeneous i.e., flat region where there is no edge. Schulze reports that noise level can also be estimated as the local standard deviation corresponding to the highest peak of the histogram of the local standard deviation of an image [67]. There, the idea is that values of the local standard deviation produced from edges shall spread throughout the histogram, while those resulting from noise shall concentrate over a narrow range of low values. When κ is estimated in relation with noise level, the authors' experience suggests to choose a value smaller than the estimation based on the local dispersion of the grey level intensity. Indeed, as time t increases, noise level decreases and some edges may be removed if κ is too high. This is all the more true that κ is a soft gradient threshold. More precisely, the *bascule* between the two regimes (high diffusion versus low / inverse diffusion) is not sharp but occurs over a range of edge slopes (Figure 4 and Figure 5). In any case, tuning κ necessitates a bit of practice. Other heuristic strategies from those recalled above may be preferred including the manual trial and error approach on sub images.

2.4.3.3 Stability of the nonlinear filter

It shall be acknowledged that the proposed solution for local contrast steepening has been qualified by some as an unstable process i.e., an ill-posed process, which can amplify noise and/or generate ripples [72] [73] [74] [75] [76] [77] [78]. From the mathematical point of view i.e., within the variational formalism whereby Eq. 4 is expressed as the minimization of an energy surface [68] [79], these authors are right. Indeed, Eq. 4 can be qualified as ill-posed when using either of the diffusion functions in Eq. 5 or Eq. 12. Ill-posedness is reflected in Eq. 7 where the directional coefficient $b = c + \|\boldsymbol{\nabla} u\| \, c'$ normal to the isolines of u turns negative where $\|\boldsymbol{\nabla} u\|_{(\mathbf{x},t)}$ is high in the vicinity of the steepest region of a marked edge (Figure 4.B and Figure 5.B). The mathematical view point being acknowledged, let us consider the practical viewpoint. Practically, the simple discretization of Eq. 4 in the form of Eq. 10 using *unstable* diffusion functions (Eq. 5 or Eq. 12) is found numerically stable. This stable behavior may be explained by the maximum principle [39] in the original sense of Nirenharg [80].

For sake of completeness, two stable diffusion functions are provided below. When fitted in Eq. 4, these functions make the diffusive process mathematically well-posed. A stable diffusion function is a diffusion function c whose associated weighting coefficient $b = c + \|\boldsymbol{\nabla} u\| \, c'$ normal to the isolines of u remains positive in the vicinity of a marked edge. The first stable diffusion function (Eq. 13) has been proposed by Green [81] (see also Tschumperlé and Deriche [82]) and the second (Eq. 14) is due to Charbonnier et al. [83].

$$c(\|\nabla u\|)_{(\mathbf{x},t)} = \frac{\tanh\left(\frac{\|\nabla u\|}{\kappa}\right)}{\kappa\|\nabla u\|} \qquad \text{Eq. 13}$$

$$c(\|\nabla u\|)_{(\mathbf{x},t)} = \frac{1}{\kappa^2\sqrt{\left(1+\frac{\|\nabla u\|^2}{\kappa^2}\right)}} \qquad \text{Eq. 14}$$

In the authors' opinion, these two stable diffusion functions, which only preserve but do not sharpen step-edges are far less appropriate than unstable functions (Eq. 5 or Eq. 12) within the current quest for improved contrast.

2.4.3.4 Binarization

After nonlinear contrast enhancement, all subsequent digital image processing was done in the Aphelion Dev environment.

After application of the nonlinear filter reviewed above, the filtered images $u(\boldsymbol{x},t)$ were typified by a high enough *contrast ratio* between *objects* (foreground) and the background. This allowed to binarize all samples by a simple direct threshold of the grey level histogram (with no need to have any skills in image processing) e.g., Figure 6.A.

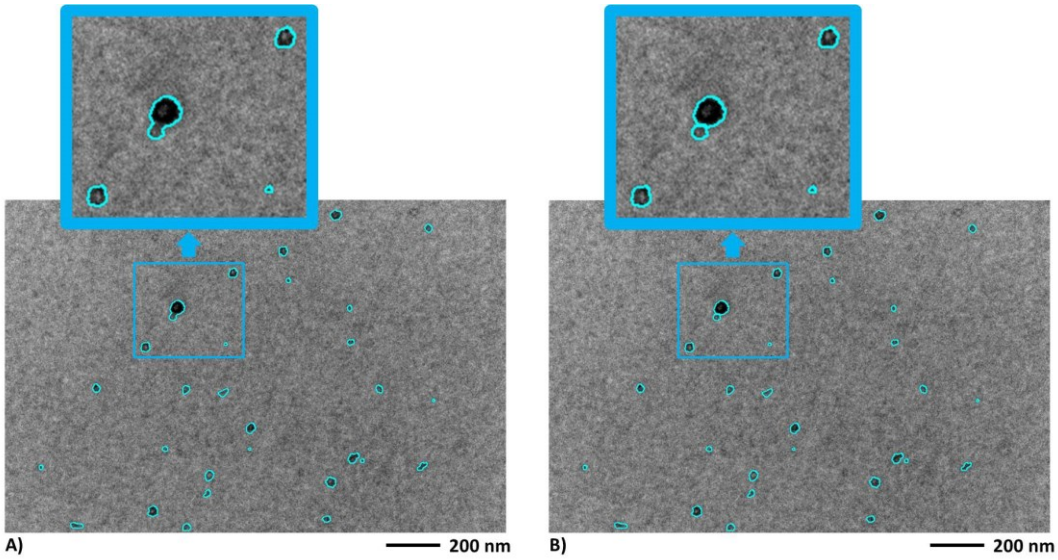

Figure 6. Automatic binarization of micellar objects sampled in a TEM micrograph of a 99.75/0.25 wt% PMMA/MAM blend precursor (see also Figure 1 at a higher magnification). **A)** After running the nonlinear directional filter (Eq. 4) over the original image $u_{(\mathbf{x})}$ to sharpen contrast, nanostructures in the filtered image $u(\boldsymbol{x},t)$ could be segmented by a simple threshold of the grey level histogram. In this display, the level set corresponding to the threshold value is superimposed in cyan upon the original image. **B)** Automatic disconnection of overlapping nanostructures in A) (see the insets).

Before thresholding, the filtered image $u_{(\mathbf{x},t)}$ was if necessary corrected for shading (uneven background matrix) using division of the filtered mage by a *bright image* according to Eq. 15. Then, the relevant grey level cut-off value could be searched manually or in an automated way, for example, in the manner of Kapur et al. as the grey-level that maximizes the entropy of the grey-level histogram [84]. Figure 6.A illustrates the automatic binarization step.

$$u_{(\mathbf{x},t)}^{Corrected} = \frac{u_{(\mathbf{x},t)}}{blank_{(\mathbf{x},t)}} \times C \qquad \text{Eq. 15}$$

where the blank field image $blank_{(\mathbf{x},t)}$ is built by convolving $u_{(\mathbf{x},t)}$ by a large Gaussian kernel and C is a normalization constant.

2.4.3.5 Local size measurements

In a binarized image, adjacent nanostructures may touch or partially overlap (see inset in Figure 6.A). Instances of this should be considered for an appropriate statistical characterization of the size of the segmented elementary nanostructures. Where necessary, overlapping nanostructures should therefore be separated before performing local size measurements. A region growing approach was used to deal with partitioning of mingled nanostructures [85].

More precisely, a seeded watershed decomposition of the gradient transform of the binary image was performed [86] [87]. The markers of the objects (the seeds) were the minima of the inverse of the distance function. This algorithm requires hole filling as a prerequisite. Thus, holes (including the core of the segmented core-shell nanostructures) were filled by applying a closing by reconstruction. Efficiency of the splitting algorithm is illustrated in Figure 6.B.

After automatic disconnection of overlapping objects, the binary images were perfectly suited to the automatic measurement of object sizes The diameter $D(O)$ of every object O was automatically derived from measurement of the object perimeter $P(O)$ ($D = \frac{P}{\pi}$). As recalled elsewhere [88], measuring the perimeter is not an easy matter in a digital 2D image. Simple methods such as counting the number of boundary pixels lead to important errors. As an alternative, the Crofton method was used. As expressed by Eq. 16 in the Euclidean space, the Crofton method is based on integrating for all affine lines L in the plane the Euler-Poincaré characteristic χ of $O \cap L$, where $O \cap L$ is the intersection of the line L with the object O [89] [90].

$$P(O) = \pi \int_{\mathcal{L}^2} \chi(O \cap L) dL \qquad \text{Eq. 16}$$

Where $\mathcal{L}^2$ is the set of all affine lines L in the plane, and where the Euler-Poincaré characteristic χ is half the intercept number of object O with lines of various orientation and position.

The Crofton formula (Eq. 16) is easy to apply to digital binarized images [89] [90] [91]. The integral over lines in Eq. 16 is decomposed into a sum over a finite set of directions and a sum over all lines parallel to each direction. The perimeter was numerically estimated by considering horizontal and vertical lines and also the diagonals (four directions) as:

$$P(O) \approx \frac{\pi}{4} \sum_{k=1}^{4} \frac{\chi(O \cap L_k)}{\lambda_k} \qquad \text{Eq. 17}$$

where λ_k is the density of the lines in direction k and L_k is the set of all discrete lines in direction k. The density λ_k is computed as the ratio of the distance between two neighbor pixels with the area of a pixel. It takes a value of 1 in the horizontal and vertical directions against $\sqrt{2}$ along the diagonals.

Using Eq. 17, the diameter of each and every of the objects (O) segmented in an image could be estimated as $D(O) = \frac{P(O)}{\pi}$ and the object size (diameter) distribution could be determined in a fully automatic manner.

3. RESULTS AND DISCUSSION

Fully automated image analysis methods are capable of delineating very rapidly a very large number of objects. Yet, in some instances, they may lead to imprecise structural characterization of multiphase materials. In such instances, this is almost always due to the ubiquitous inhomogeneous and/or *deficient* contrast ratio between phases, which is a major source of possible error in any automatic binarization [50]. On the other hand, representative structural statistical characterizations are difficult to achieve otherwise than via the automated route. In this sense, the nonlinear diffusive filter reviewed above, deemed to further enhance contrast between phases, shall promote the *safe* use of fully automatic methods. In what follows, this versatile filter is applied to images of multiphase acrylate micro-nano structured materials before and after $scCO_2$ foaming. It is shown that after running the filter, the solution image can be accurately binarized by a simple threshold of the histogram. Representative statistical size distribution of the objects (BCP nanostructures and foam cells) are then derived from the binarized images.

The PMMA/MAM systems illustrated in this study are typified by a MAM content ranging from 0.25 wt% to 10 wt%. All blend precursors show nanosized phase-separated BCP domains dispersed in the PMMA matrix, although these domains are out-of-equilibrium. This is consistent with Bernardo et al. who observed phase separation down to 0.1 wt% of MAM [24] i.e., close to the CMC for these blends. One purpose of using a very low amount of MAM is to decrease noticeably the relative density of the final foam [24].

3.1 Nanostructuration of the solid blends

Figure 7 illustrates the proposed numerical strategy for edge enhancement in the case of the solid 99.75/0.25 wt% PMMA/MAM blend precursor shown in Figure 1. When the nonlinear diffusive filter is run over a large enough time t, the achieved solution $u_{(\mathbf{x},t)}$ tends to a piecewise constant solution (Figure 7). It shall be noted that such piecewise constant solution image (Figure 7) is rather different from the original continuous image $u_{(\mathbf{x})}$ (Figure 1). This distinctive feature has been criticized by some [63] and it is important to address this issue. Here, the main point is not to improve the quality of the original image $u_{(\mathbf{x})}$. The aim is to propose a solution image $u_{(\mathbf{x},t)}$, which eases the subsequent

automatic binarization step. In this sense, reconstructing a *virtual image* such as Figure 7, which represents a simplified image at a lower resolution with sharper step-edges separating clearly phases is here the very goal. Indeed, this eases greatly the subsequent binarization. In other words, a piecewise constant image such as Figure 7 may be viewed as *already closer to* the target binary image (which is also piecewise constant) than to the original image.

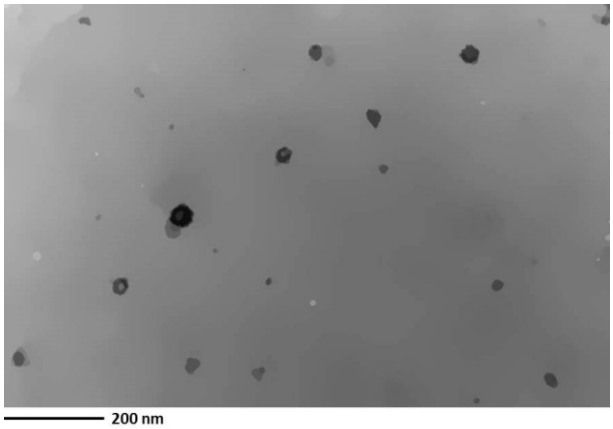

Figure 7. TEM micrograph of a 99.75/0.25 wt% PMMA/MAM dense blend after applying to Figure 1 the nonlinear diffusive filter given in Eq. 4. Gaussian blurring (isotropic linear diffusion) applies selectively to flat regions (PMMA matrix) which are dissipated, while the boundaries and the contrast of the nanostructures are enhanced with increasing time t i.e., when decreasing the resolution of the original image.

In the sharpened image in Figure 7 (where dispersion of the grey level intensity u is now mostly explained by enhanced step-edges between homogenized phases), the segmentation of nanostructures standing out plainly from a *flat* background becomes straightforward. Segmentation was accomplished through a simple threshold of the grey level histogram (Figure 8).

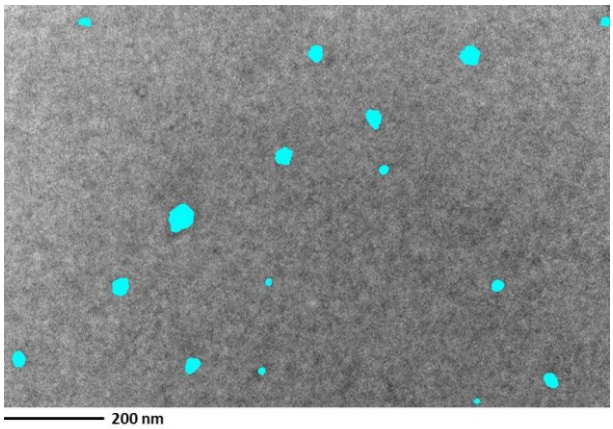

Figure 8. Binarized (0 -1) counterpart of the grey level image shown in Figure 7 using a simple threshold of the grey level histogram. The segmented nanostructures (labeled with a 1 value) are displayed in cyan, superimposed upon the original image (Figure 1) rather than leaving in transparency the 0-valued background PMMA matrix.

Note that in Figure 8, a filter based on connectivity i.e., an opening by reconstruction (a filter which preserves contours [92]) was run after thresholding to remove the smallest *islands* considered as noise in the binarized image.

For robust statistics, several micrographs acquired at different magnifications were systematically binarized e.g., Figure 6 and Figure 8. This enabled calculation of the diameter of several thousand nanostructures for this sample. The resulting size distribution is given in Figure 9.

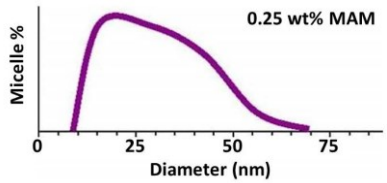

Figure 9. Size distribution of micellar objects (99.75/0.25 wt% PMMA/MAM dense blend precursor) automatically determined from binarized TEM micrographs e.g., Figure 6.B and Figure 8. In this display, the finite size interval bins of the frequency histogram of the nanostructure diameters are schematically represented as a continuous distribution of the nanostructure percentile as a function of nanostructure size. The vertical full scale is set to the highest micelle percentile of the original frequency histogram. The average size of the nanostructure derived from this statistical distribution is $\overline{D}_{nanostructure} = 27\ nm\ \pm 1\ nm$.

Availability of the representative statistical size distribution given in Figure 9 is a central point for understanding and optimizing the foaming process. For example, it is well known that overlapping between cell nucleation and growth during foaming shall be minimized, in particular in view of producing *all nanosized* foams [20] [93] [94] [95] [96]. From Figure 9, one can confidently argue that the relative narrowness of the nanostructure size distribution shall contribute to minimize any potential overlap time between cell nucleation and growth during foaming. That is to say, from the compounding viewpoint, the observed tight size distribution of the nucleants (Figure 9) supports that the latter shall activate over a very short time interval and grow all together to a fairly uniform cell size [97] [98].

Figure 10.A shows a TEM micrograph of a (PTA-stained) PMMA/MAM solid precursors with a higher MAM content (10 wt%) than in Figure 1. Interestingly, Figure 10.A supports that coloration by liquid diffusion such as PTA liquid staining produces essentially a surface selective staining. PTA would preferentially rise from the nanostructures intercepted by the ultra-thin slice surface so that *surface-nanostructures* are the most contrasted. Since nanostructures essentially do not percolate downwards i.e., do not form continuous *flow paths* for PTA through the thickness of the slice, nanostructures deeper-lying in the thickness would be hardly or not at all colored (Figure 10.A). In such an instance, the derivation of the nanostructures volumetric number density $N_{nanostructure}$ (number of nanosized domains/cm^3) shall be based on the stereological formula given in Eq. 18, where n is the number of surface-nanostructures segmented in an image and A is the area of the digital image in cm^2.

$$N_{nanostructure} = \left(\frac{n}{A}\right)^{3/2} \qquad \text{Eq. 18}$$

The proposed method of image optimization by selective local contrast enhancement allows to straightforwardly and automatically binarize surface-nanostructures, consistently with the stereological formula given in Eq. 18. As shown in Figure 10.B, when run over a long enough time t with a high enough contrast parameter κ, the nonlinear diffusive filter leads to a piecewise constant image where only the darker surface nanostructures are preserved and further enhanced for the subsequent binarization (Figure 10.C). To achieve this, the diffusive function provided in Eq. 12 was used.

Figure 10.B clearly illustrates how information content selectively decreases towards higher levels of description (coarser resolutions). Boundaries and edges (the zero-crossings of the Laplacian of the image) *are moved* when sweeping out the scale-space image $u(\mathbf{x}, t)$ (when increasing the time-scale parameter t). In this sense, the material may be viewed as virtually reconstructed.

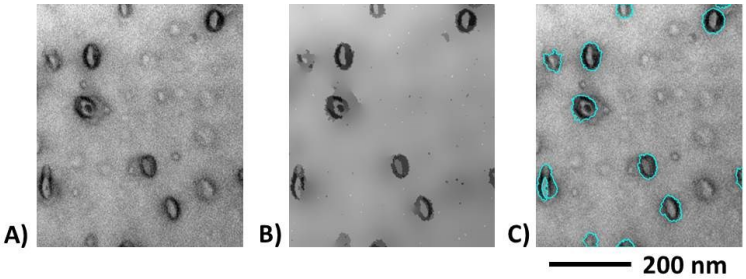

Figure 10. **A)** High magnfication TEM micrograph (local area) showing the nanostructuration of a 90/10 wt% PMMA/MAM solid blends after PTA staining. **B)** Filtered image representing a simplified image at a coarser resolution with sharper boundaries after running over the original micrograph the nonlinear filter (Eq. 4) using the diffusion function in Eq. 12. **C)** Segmented counterpart of image B) by simple thresholding of the grey level histogram. The level set corresponding to the threshold values is superimposed in cyan upon the original images A).

This method of image optimization can be applied to many other polymer blends e.g., SBS, SEBS, SMA, SMMA or composites doped with nanocharges such as carbon nanotubes or nano clays, including systems with smoother interfaces (interphases) as encountered for example in high magnification TEM images of polyolefin blends [27]. In the latter case, the soft gradient threshold κ entering in the definition of the diffusion function should take a value lower than the edge slope of the smooth surface between inclusions and matrix. Yet, a too low value for κ may carry with it the possible risk of enhancing also noise.

More generally, the efficiency of the method shall depend upon the upstream steps determining the initial level of contrast: on the one hand, the contrast method e.g., RuO_4 vapor stain, RuO_4 liquid stain, OsO_4 staining, PTA liquid stain or *n*-hexane etching [27] [48] [53] [54] [55] [99], and on the other hand, the imaging method (e.g., SEM, TEM, energy filtered TEM, atomic force microscopy (AFM) or confocal scanning laser microscopy), whose choice is material dependent. In any case, the proposed method of interface/interphase enhancement, operating downstream in the contrast formation chain, is far less material-dependent than the upstream staining and imaging stages.

3.2 Cellular structure

Figure 11 is another illustration of the general interest of the proposed image optimization method for local contrast ratio enhancement. The filtered image (Figure 11.B) is, here again, a piecewise constant solution representing a simplified image at a lower resolution with sharper interfaces between foam cells and solid lattice. At cell walls, the ridge contrast contributing to the overall topographical contrast (cf Section 2.4.2) is clearly heightened. The darker grey levels, which typify cells floor (due to combined shading and inclination contrast contributions to the overall contrast; Section 2.4.2), are smoothed and lowered. The subsequent segmentation of foam cells standing out from a much brighter solid lattice could be accomplished via a simple threshold of the grey level histogram (Figure 12).

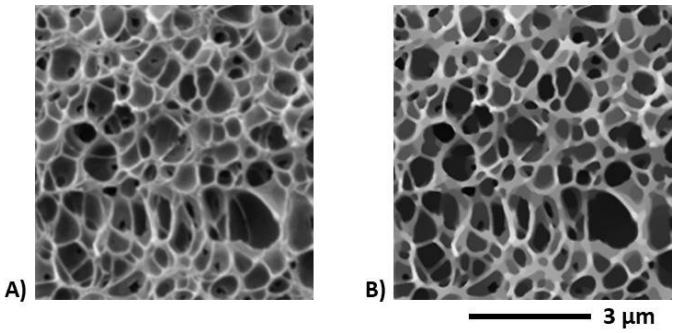

Figure 11. **A)** Local zoom (see blue blox in Figure 2) in a SEM micrograph of a foam produced from 99.75/0.25 wt% PMMA/MAM precursor (Figure 1) at a $scCO_2$ pressure of 30 MPa and at 60°C for the saturation stage and using a pressure drop rate of 0.5 MPa/s. **B)** Local zoon in the enhanced image after applying to Figure 2 the nonlinear diffusive filter given in Eq. 4 and Eq. 5. Gaussian blurring applies selectively to flat intra-phase regions, which are homogenized, while interphase contrast is further steepened

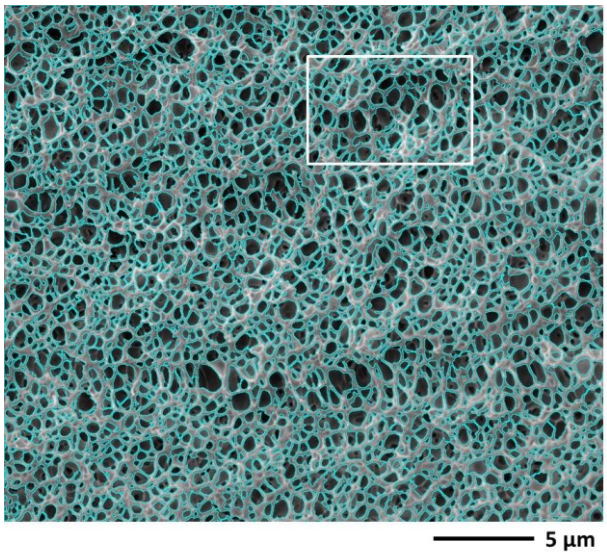

Figure 12. Binarized counterpart of the grey level image $u(\mathbf{x}, t)$ locally illustrated in Figure 11.B by simple thresholding of the histogram. The level set corresponding to the threshold value is superimposed in cyan upon the original image $u(\mathbf{x})$ (Figure 2). See Figure 13 for the white box.

Contiguous cells are highly interconnected in this series of open foams. The numerous instances of this were systematically considered for an accurate statistical characterization of cell sizes. Touching pores were separated using the region growing approach recalled in section 2.4. The efficiency of the splitting strategy is illustrated in Figure 13. After partitioning of mingled objects (pores), object sets like the one in Figure 12 were appropriate for measurement of the cell size distribution (Figure 14).

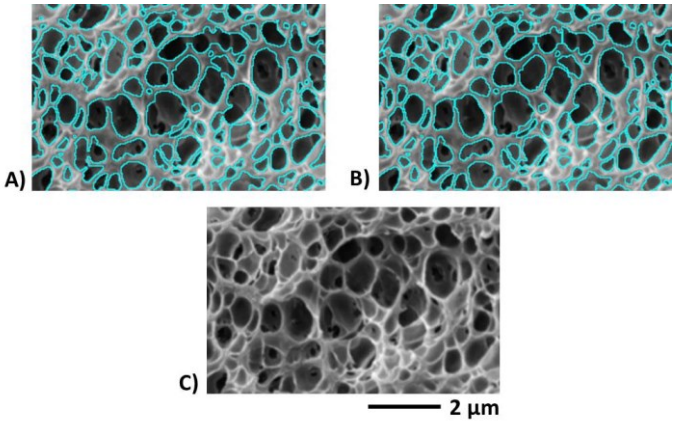

Figure 13. Partitioning of mingled pores. Close-up of the area bounded by the white box in Figure 12. The porosity segmented by thresholding the grey level histogram of the filtered image is represented in cyan in Figure 13.A superimposed upon the original image (Figure 13.C). Figure 13.A is not yet appropriate for the statistical characterization of pore sizes, since numerous individual pores touch or overlap. Touching/overlapping cells in Figure 13.A must be separated before performing size measurement. This is done in Figure 13.B relying on the standard region growing approach recalled in section 2.4.

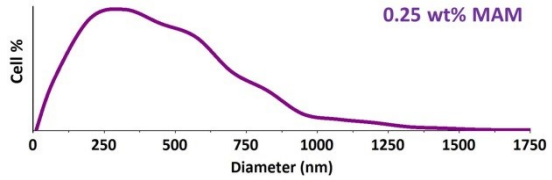

Figure 14. Cell size distribution of a foam (Figure 2) produced from a 99.75/0.25 wt% PMMA/MAM blend precursor (Figure 1) The size distribution was determined from the binarized micrograph in Figure 12. The average size of the cells derived from this statistical distribution is $\overline{D}_{cell} = 461\ nm\ \pm 54\ \ nm$.

The proposed approach is particularly well suited to the characterization of multimodal samples including different scales of porosity. Figure 15 shows a foam produced from a 99.5/0.5 wt% PMMA/MAM precursor. The qualitative appraisal of Figure 15 indicates occurrence of a twofold porosity made up of two cell populations of quite different size and number density. In such an instance, carrying cell size characterization at a single resolution (e.g., that of Figure 15) would be at the expense of representativeness (by number) for the larger cells, far less numerous than the smaller ones. Relying on the proposed nonlinear filter, the quantitative calculation of the size distribution of the large cell population (Figure 16) was performed over a lower magnification SEM micrograph (Figure 17) for the robust sampling of large objects.

The observed discrete occurrence of larger cells in this foam sample (Figure 15 and Figure 17) produced from a 99.5/0.5 wt% PMMA/MAM solid blend precursor may be explained as follows: when effective nanostructures are too few (low MAM content in the precursor) they may not allow to depress rapidly enough supersaturation by cell growth at nanostructures sites. In this situation, homogeneous nucleation may locally occur in parallel with heterogeneous nucleation [98].

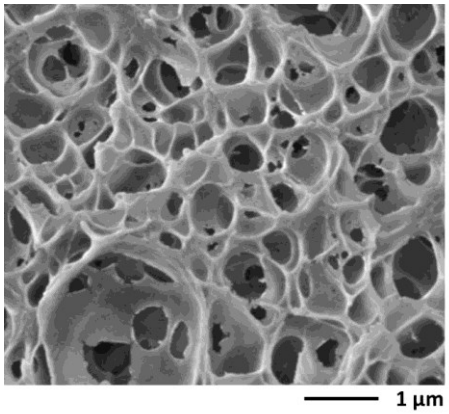

Figure 15. Cellular structure of a foam produced from a 99.5/0.5 wt% PMMA/MAM blend precursor at a $scCO_2$ pressure of 30 MPa and at 60°C for the saturation stage and using a pressure drop rate (PDR) of 0.5 MPa/s.

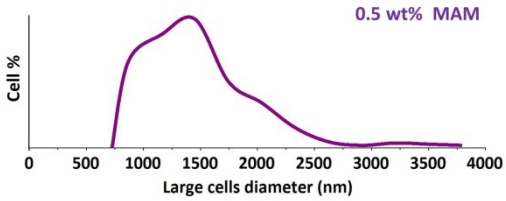

Figure 16. Cell size distribution of the large cell population locally illustrated in Figure 15. The size distribution was determined on a low magnification micrograph (Figure 17) for the robust sampling of the quite sparse large objects (~ 1% by number of all cells). The average size of this large-sized cell population derived from the statistical size distribution is $\overline{D}_{large\ cell} = 1490\ nm$.

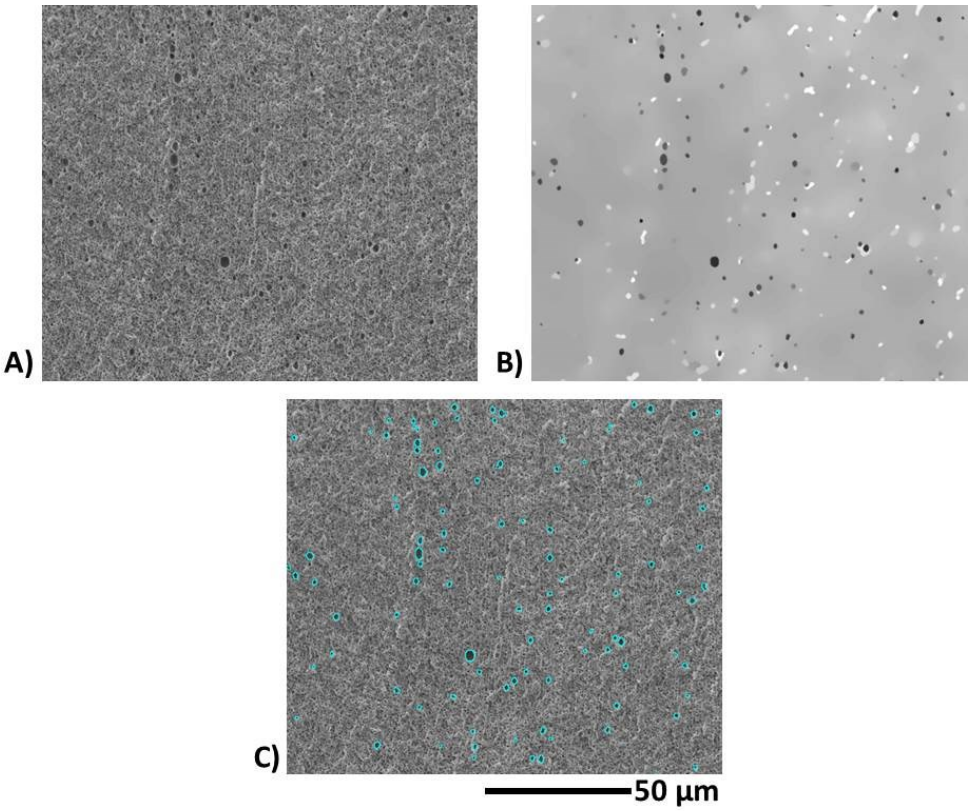

Figure 17. Binarization of the large-sized cell population in a bimodal foam including numerous small-sized cells and sparse large-sized cells, both dispersed in a solid polymeric lattice. The sample was produced from a 99.5/0.5 wt% PMMA/MAM acrylic precursor at a $scCO_2$ pressure of 30 MPa and 60°C for the saturation stage, followed by a PDR of 0.5 MPa/s to trigger

foaming. **A)** Original low magnification SEM micrograph $u(\mathbf{x})$ (local zone) **B)** Filtered micrograph $u(\mathbf{x}, t)$. The contrast of large objects is clearly enhanced after applying to A) the diffusive filter of interest to this paper. Flat regions (greyish / speckle background formed by the poorly small cell population at this low magnification) are selectively homogenized. In this display, the filtered micrograph $u(\mathbf{x}, t)$ was post processed by standard histogram stretching to better visualize the beneficial action of the filter. **C)** Binarized (0 – 1) counterpart of the filtered image in B) after simple thresholding. The segmented large-sized cells are displayed in cyan, superimposed upon the original image A). The cell size distribution of the segmented objects is given in Figure 16.

Figure 18 illustrates the exactness of labeled (segmented) void cells using the proposed approach. The porous material in Figure 18 was foamed from a 90/10 PMMA/MAM acrylate blend precursor. It includes both nanosized and microsized porous cells. This two-scale structuration, observed at a *high* MAM content of 10 wt%, is most probably produced by serial nucleation mechanisms and is expected to be advantageous for thermal insulation applications [20].

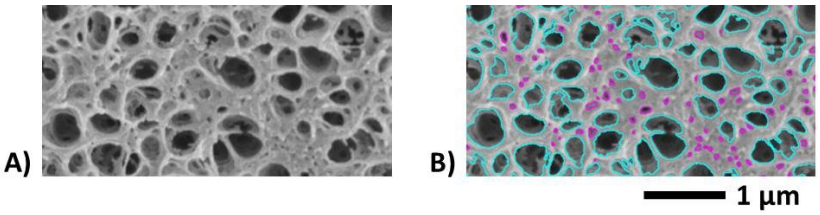

Figure 18. **A)** Local illustration of a foam sample produced from a 90/10 wt% PMMA/MAM solid precursor saturated with $scCO_2$ at 40°C and 30 MPa and foamed in one-step batch foaming with a PDR of 0.5 MPa/s. **B)** Segmented cells include inter skeletal microsized pores (in cyan) versus intra skeletal nanosized pores (in magenta). Such an accurate delineation of bimodal micro-nano cells could be achieved relying on the nonlinear diffusive filter reviewed in this work.

To all intents and purposes, the proposed methodology is as an efficient, versatile and simple alternative solution (only four parameters need to be set) to accurately evaluate the size and density of objects (nanostructures, porous cells) across digital images at several scales, taking into account a very large number of objects.

4. CONCLUSION

Understanding the respective impact of material formulation (e.g., block copolymer (BCP) content and size) and process factors for optimizing a foaming process is largely facilitated when the structuration of the *input* and *output* materials (which can be qualitatively appraised in digital micrographs) are quantified in terms of representative statistical size distributions. Examples are given in this work for both the nanostructures (BCP) in the unfoamed precursor and the porous cells in the final foam. Structural characteristics derived from those size distributions e.g., average cell size and cell number density are then of great help to correlate the micro-nano porous structure to the physical properties of the foam.

Prior to calculating the size distribution of an object set (BCP nanostructure or porous cell), the latter must be accurately segmented. In most instances, this is a tedious procedure (since the appropriate image treatment is in general image-dependent), which also requires specific skills in image analysis. An alternative route is proposed in this work. It consists in enhancing first the contrast of the object set sampled in a (series of) digital micrograph(s), so that the subsequent automatic segmentation is as simple as possible e.g., simple threshold of the grey level intensity histogram.

To do so, a multiscale (multiresolution) description of electronic images is assumed. The selected approach builds on the so-called scale-space filtering. According to this formalism, the original image is filtered over coarser resolutions (larger scale levels of description) relying on a diffusion process whereby the local grey level intensity spreads across the image pixels. More precisely, a nonlinear scale-space is used where diffusion of the grey level intensity is directional and locally adaptive to image data.

The application of this approach to polymer science is new to the best of the authors' knowledge. In the use made here of this approach, what may has been perceived as a weakness in other disciplinary fields (e.g., image denoising or image restoration) is put to profitable use.

Running over a digital grey level image this directional adaptive diffusion equation is shown to lead to efficient enhanced reconstructions of the objects of interest (nanostructures or pores) at large values of the time t of the diffusive process. The solution image is shown to ease greatly the subsequent automatic segmentation step and calculation of representative size distributions. The intent of the authors is that this methodology can be useful to and further applied to polymer science.

Several physical insights may be drawn from the phase-separation morphology quantifications illustrating this methodological work.

At low MAM content, close to CMC, the PMMA/MAM systems show a tight size distribution of phase-separated BCP domains (Figure 9). This shall a priori favor nucleants activating over a very short time interval and growing in tandem during one-step $scCO_2$ batch foaming, leading thereby to lightweight foams of uniform cell size. This expectation is here only qualitatively met, as revealed by the somewhat loose cell size distribution in Figure 14 due to use of a rather high saturation temperature ($T_{sat} = 60°C$), which does not minimize cell growth and coalescence. This substantiates all the interest of disposal of representative size distributions for understanding and optimizing a foaming process.

TEM observations (Figure 10.A) support that PTA liquid stain of the soft PBA block of MAM would be mostly a surface selective coloration. The current method of image optimization permits to segment straightforwardly the surface nanodomains (Figure 10.B and Figure10.C) and thereby, to assess consistently the nanodomains volumetric number density using the stereological formula in Eq. 18. The issue of using a stereological framework for quantifying nanodomains in liquid stained TEM preparations of PMMA/MAM blends has never been raised to the best of the authors' knowledge.

The approach is very suited to the characterization of multimodal samples including different scales of porosity. Close to CMC, bimodality is most probably ascribed to parallel nucleation mechanisms. At higher MAM content, the accurately delineated bimodality (Figure 18) reflects serial nucleation mechanisms [20].

Supporting Information: Numerical discretization

Acknowledgements

This work was supported by the Agence Nationale de la Recherche (ANR, France) AAPG PRCE 2018CE06 0030, 2019; ANR is gratefully acknowledged. We thank Anne-Valérie Ruzette and the Laboratoire Matière Molle et Chimie (Paris France) for fruitful exchanges on staining procedures of acrylic blends prior to TEM observations. We thank Sabrina Lacomme and the Bordeaux Imaging Center (Bordeaux, France) for assistance in TEM observations. We thank Stephanie Reynaud (Laboratoire Hubert Curien, Saint Etienne, France) and the SEMPA for valuable advices on use of EF-TEM as a technical solution to contrast enhancement.

REFERENCES

(1) Fresco-Cala, B.; Cárdenas, S. Advanced polymeric solids containing nano- and micro-particles prepared via emulsion-based polymerization approaches. A review. *Analytica Chimica Acta* **2022**, *1208*, 339669. https://doi.org/10.1016/j.aca.2022.339669

(2) Xu, X.; Bizmark, N.; Christie, K. S. S.; Datta, S. S.; Ren, Z. J.; Priestley, R. D. Thermoresponsive polymers for water treatment and collection. *Macromolecules* **2022**, *55*, 1894–1909. https://doi.org/10.1021/acs.macromol.1c01502

(3) Osaka, N.; Takeda, N.; Adachi, M.; Okufuji, M.; Osaka, R. Miscibility, hierarchical structures, and enhanced mechanical properties of acrylic rubber by the formation of a chemically and physically crosslinked partially miscible interpenetrating polymer network with poly(vinylidene fluoride). *Macromolecules* **2023**, *56*, 1419–1433. https://doi.org/10.1021/acs.macromol.2c02147

(4) Lynd, N. A.; Meuler, A. J.; Hillmyer, M. A. Polydispersity and block copolymer self-assembly. *Progress in Polymer Science* **2008**, *33*, 875–893. doi: 10.1016/j.progpolymsci.2008.07.003

(5) Zhang, T.; Sanguramath, R. A.; Israel, S.; Silverstein, M. S. Emulsion templating: Porous polymers and beyond. *Macromolecules* **2019**, *52*, 5445−5479. DOI: 10.1021/acs.macromol.8b02576

(6) Steube, M.; Johann, T.; Barent, R. D.; Müller, A. H. E.; Frey, H. Rational design of tapered multiblock copolymers for thermoplastic elastomers. *Progress in Polymer Science* **2022**, *124*, 101488. https://doi.org/10.1016/j.progpolymsci.2021.101488

(7) Chen, J. Advanced electron microscopy of nanophased synthetic polymers and soft complexes for energy and medicine applications. *Nanomaterials* **2021**, *11*, 2405. https://doi.org/10.3390/nano11092405.

(8) Zielinski, M.; Röder, C.; Schröder, G. F. Challenges in sample preparation and structure determination of amyloids by cryo-EM. *Journal of Biological Chemistry* **2021**, *297* (2), 100938. https://doi.org/10.1016/j.jbc.2021.100938

(9) Wang, Y.; Sun, M.; Zhang, H.; Lu, Y.; You, W.; Bian, F.; Yu, W. Quantitative correlation between hierarchical nanofiller structure and rheology of polymer/fumed silica nanocomposites. *Macromolecules* **2023**, *56*, 934–946. https://doi.org/10.1021/acs.macromol.2c02080

(10) Park, S. J.; Bates, F. S.; Dorfman, K. D. Complex phase behavior in binary blends of AB diblock copolymer and ABC triblock terpolymer. *Macromolecules* **2023**, *56*, 1278−1288. https://doi.org/10.1021/acs.macromol.2c02216

(11) Galloway, J. A.; Montminy, M. D.; Macosko, C. W. Image analysis for interfacial area and cocontinuity detection in polymer blends. *Polymer* **2002**, *43*, 4715–4722. https://doi.org/10.1016/S0032-3861(02)00282-3

(12) López-Barrón, C. R. ; Macosko, C. W. Characterizing interface shape evolution in immiscible polymer blends via 3D image analysis. *Langmuir* **2009**, *25* (16), 9392–9404. DOI: 10.1021/la803450y

(13) López-Barrón, C. R. ; Macosko, C. W. Measurement of geometrical parameters in cocontinuous polymer blends: 3D versus 2D image analysis. *Journal of Microscopy* **2011**, *242*, Pt 3, 242–249. doi: 10.1111/j.1365-2818.2010.03462.x

(14) Behling, R. E.; Wolf, L. M.; Cochran, E. W. Hierarchically ordered montmorillonite block copolymer brushes. *Macromolecules* **2010**, *43*, 2111–2114, DOI: 10.1021/ma902357s

(15) Gong, X.; Gnanasekaran, K.; Chen, Z.; Robison, L.; Wasson, M. C.; Bentz, K. C.; Cohen, S. M.; Farha, O. K.; Gianneschi, N. C. Insights into the structure and dynamics of metal–organic frameworks via transmission electron microscopy. *Journal of the American Chemical Society* **2020**, *142*, 17224−17235. https://dx.doi.org/10.1021/jacs.0c08773

(16) Gardner, W.; Winkler, D. A.; Muir, B. W.; Pigram, P. J. Applications of multivariate analysis and unsupervised machine learning to ToF-SIMS images of organic, bioorganic, and biological systems. *Biointerphases* **2022**, *17*, 020802. doi: 10.1116/6.0001590.

(17) Vitali, C.; Peters, R. J. B.; Janssen, H.-G.; Nielen, M. W. F.; Ruggeri, F. S. Microplastics and nanoplastics in food, water, and beverages, part II. Methods. *Trends in Analytical Chemistry* **2022**, *157*, 116819. https://doi.org/10.1016/j.trac.2022.116819

(18) Zhang, L.; Shao, S. Image-based machine learning for materials science. *Journal of Applied Physics* **2022**, *132*, 100701. doi: 10.1063/5.0087381.

(19) Kainourgios, P.; Maroulas, P.; Charitidis, C. A. Effect of crosslinker to monomer ratio on the adhesion and size distribution of silver nanoparticles grown on poly (methacrylic acid) microspheres. *Colloids and Surfaces A: Physicochemical and Engineering Aspects* **2023**, *662*, 131002. https://doi.org/10.1016/j.colsurfa.2023.131002

(20) Haurat, M. ; Anguy, Y. ; Gaborieau, C. ; Aubert, G. ; Aymonier, C. ; Dumon, M. High-pressure drop rates in solid-state batch one-step $scCO_2$ foaming of acrylic polymers: a way to stabilize the structure of micro-nano foams. *Chemical Engineering Science* **2023**, *281*, 119099. DOI: https://doi.org/10.1016/j.ces.2023.119099

(21) Dumon, M. ; Ruiz, J. A. R. ; Sanz, J. P. ; Perez, M. A. R. ; Tallon, J.-M. ; Pedros, M. ; Cloutet, E. ; Viot, P. Block copolymer-assisted microcellular supercritical CO_2 foaming of polymers and blends. *Cellular Polymers* **2012**, *31* (4) 207–222, doi:10.1177/026248931203100402

(22) Pinto, J.; Dumon, M.; Pedros, M.; Reglero, J.; Rodriguez-Perez, M. A. Nanocellular CO_2 foaming of PMMA assisted by block copolymer nanostructuration. *Chemical Engineering Journal* **2014**, *243*, 428–435. http://dx.doi.org/10.1016/j.cej.2014.01.021

(23) Pinto, J.; Reglero-Ruiz, J. A.; Dumon, M.; Rodriguez-Perez, M. A. Temperature influence and CO_2 transport in foaming processes of poly(Methyl Methacrylate)–block copolymer nanocellular and microcellular foams. *J. Supercrit. Fluids* **2014**, *94*, 198–205. http://dx.doi.org/10.1016/j.supflu.2014.07.021

(24) Bernardo, V.; Martin-de Leon, J.; Pinto, J.; Catelani, T.; Athanassiou, A.; Rodriguez-Perez, M. A. Low-density PMMA/MAM nanocellular polymers using low MAM contents: Production and characterization. *Polymer* **2019**, *163*, 115–124. https://doi.org/10.1016/j.polymer.2018.12.057

(25) Bernardo, V. ; Martin-de Leon, J. ; Rodriguez-Perez, M. A. Highly anisotropic nanocellular polymers based on tri-phasic blends of PMMA with two nucleating agents. *Materials Letters* **2019**, *255*, 126587, doi: 10.1016/j.matlet.2019.126587

(26) Haurat, M.; Dumon, M. Amorphous polymers' foaming and blends with organic foaming-aid structured additives in supercritical CO_2, a way to fabricate porous polymers from macro to nano porosities in batch or continuous processes. *Molecules* **2020**, *25*, 5320. doi: 10.3390/molecules25225320

(27) Kock, C.; Gahleitner, M.; Schausberger, A.; Ingolic, E. Polypropylene/polyethylene blends as models for high-impact propylene–ethylene copolymers, Part 1: Interaction between rheology and morphology. *Journal of Applied Polymer Science* **2013**, *128* (3), 1484–1496. DOI: 10.1002/APP.38289

(28) Miyata, T.; Takagi, T.; Higuchi, J. I.; Uragami, T. Two types of fractal dimensions for phase separation in multicomponent polymer membranes. *Journal of Polymer Science, Part B: Polymer Physics* **1999**, *37* (13), 1545–1550. https://doi.org/10.1002/(SICI)1099-0488(19990701)37:13<1545::AID-POLB21>3.0.CO;2-0

(29) Xu, X.; Zhu, T. ; Van, X. ; Zhang, C. Temporal evolution of phase morphology of polypropylene/poly(ethylene octene) elastomer binary polymer blends by phase contrast microscope. *Journal of Applied Polymer Science* **2007**, *104* (5):2778–2784. DOI 10.1002/app.25648

(30) Kou, Y.; Cheng, X.; Macosko, C. W. Polymer/graphene composites via spinodal decomposition of miscible polymer blends. *Macromolecules* **2019**, *52*, 7625–7637. DOI: 10.1021/acs.macromol.9b01391

(31) Li, X.; Zhou, Z.; Keller, P.; Zeng, H.; Liu, T.; Peng, H. Interactive exemplar-based segmentation toolkit for biomedical image analysis. *Proceedings of the 2015 IEEE 12th International Symposium on Biomedical Imaging (ISBI)*, Brooklyn, NY, USA; 2015, pp. 168–171. DOI: 10.1109/ISBI.2015.7163842

(32) Arganda-Carreras, I.; Kaynig, V.; Rueden, C.; Eliceiri, K. W.; Schindelin, J.; Cardona, A.; Sebastian Seung, H. Trainable Weka Segmentation: a machine learning tool for microscopy pixel classification. *Bioinformatics* **2017**, *33* (15), 2424–2426. doi: 10.1093/bioinformatics/btx180

(33) Witkin, A.P. Scale-space filtering. *Proceedings of the 8th International Joint Conference on Artificial Intelligence*, Karlsruhe. West Germany; 1983; Vol. 2, pp. 1019–1022. https://www.ijcai.org/Proceedings/83-2/Papers/091.pdf

(34) Koenderink, J. J. The structure of images. *Biological Cybernetics* **1984**, *50* (5), 363-370. DOI: 10.1007/BF00336961

(35) Babaud, J.; Witkin, A. P.; Baudin, M.; Duda, R. O. Uniqueness of the Gaussian kernel for scale-space filtering. *IEEE Transactions on Pattern Analysis and Machine Intelligence* **1986**, *PAMI-8* (1), 26–33. DOI: 10.1109/TPAMI.1986.4767749

(36) Yuille, A.; Poggio, T. Scaling theorems for zero crossings. *IEEE Transactions on Pattern Analysis and Machine Intelligence* **1986**., *PAMI-8* (1), 15–25. DOI: 10.1109/TPAMI.1986.4767748

(37) Hummel, R. A. Representations based on zero-crossings in scale space. *Proceedings of the Conference on Computer Vision and Pattern Recognition 1986*; IEEE Computer Society, 1986, pages 204–209. ISBN: 0818607211

(38) Marr, D. *Vision: a computational investigation into the human representation and processing of visual information*; San Francisco, CA. W. H. Freeman & Co Eds, 1982. ISBN: 0716712849, 978-071671284-8

(39) Perona, P.; Malik, J. Scale-space and edge detection using anisotropic diffusion. *IEEE Transactions on Pattern Analysis and Machine Intelligence* **1990**, *12* (7), 629–639. DOI: 10.1109/34.56205

(40) Ruiz, J. A. R.; Pedros, M.; Tallon, J.-M.; Dumon, M. Micro and nano cellular amorphous polymers (PMMA, PS) in supercritical CO_2 assisted by nanostructured CO_2-philic block copolymers – One step foaming process. *The Journal of Supercritical Fluids* **2011**, *58* (1), 168–176, doi:10.1016/j.supflu.2011.04.022

(41) Bernardo, V.; Martin-de Leon, J. ; Laguna-Gutierrez, E. ; Catelani, T. ; Pinto, J. ; Athanassiou, A. ; Rodriguez-Perez, M. A. Understanding the role of MAM molecular weight in the production of PMMA/MAM nanocellular polymers. *Polymer* **2018**, *153*, 262–270, https://doi.org/10.1016/j.polymer.2018.08.022

(42) Taki, K.; Nakayama, T.; Yatsuzuka, T.; Ohshima, M. Visual observations of batch and continuous foaming processes. *Journal of Cellular Plastics* **2003**, *39* (2), 155–169. DOI: 10.1177/002195503034507

(43) Reglero-Ruiz, J. A.; Saiz-Arroyo, C.; Dumon, M.; Rodríguez-Perez, M. A.; Gonzalez, L. Production, cellular structure and thermal conductivity of microcellular (methyl methacrylate)-(butyl acrylate)-(methyl methacrylate) triblock copolymers. *Polymer International* **2011**, *60* (1) 146–152. https://doi.org/10.1002/pi.2931

(44) Gedler, G.; Antunes, M.; Velasco, J. I. Enhanced electrical conductivity in graphene-filled polycarbonate nanocomposites by microcellular foaming with sc-CO_2. *Journal of Adhesion Science and Technology* **2016**, *30* (9), 1017–1029. http://dx.doi.org/10.1080/01694243.2015.1137700

(45) Lalande, L. Structure et mécanismes de microdéformation de polyméthylméthacrylates renforcés au choc. Ph.D Dissertation, n° 3891. Ecole Polytechnique Fédérale de Lausanne, Suisse, 2007. https://doi.org/10.5075/EPFL-THESIS-3891

(46) Harris, J. R.; Ross, C.; Djalali, R.; Rheingans, O.; Maskos, M.; Schmidt, M. Application of the negative staining technique to both aqueous and organic solvent solutions of polymer particles. *Micron* **1999**, *30* (4), 289–298. DOI: 10.1016/S0968-4328(99)00034-7

(47) Pinto, J.; Dumon, M.; Rodriguez-Perez, M. A.; Garcia, R.; Dietz, C. Block copolymers self-assembly allows obtaining tunable micro or nanoporous membranes or depth filters based on PMMA; Fabrication method and nanostructures. *The Journal of Physical Chemistry C* **2014**, *118* (9) 4656–4663. DOI: 10.1021/jp409803u

(48) Ruzette, A.-V. ; Tencé-Girault, S. ; Leibler, L. ; Chauvin, F. ; Bertin, D. ; Guerret, O. ; Gérard, P. Molecular disorder and mesoscopic order in polydisperse acrylic block copolymers prepared by controlled radical polymerization, *Macromolecules* **2006**, *39*, 5804–5814. DOI: 10.1021/ma060541u

(49) Dronet, Z. Matériaux nanostructurés obtenus par combinaison de polymérisation radicalaire contrôlée et de mélangeage réactif. Ph.D Dissertation, Université Pierre et Marie Curie., Spécialité Chimie et Physique des Matériaux, 2009. https://pastel.archives-ouvertes.fr/tel-00430883

(50) Pinto, J. ; Solórzano, E. ; Rodriguez-Perez, M. A. ; de Saja, J. A. Characterization of the cellular structure based on user-interactive image analysis procedures. *Journal of Cellular Plastics* **2013**, *49* (6) 555–575. DOI: 10.1177/0021955X13503847

(51) Abràmoff, M. D.; Magalhães, P. J.; Ram, S. J. Image processing with ImageJ. *Biophotonics International* **2004**, *11* (7), 36–42. ISSN: 1081-8693

(52) Haurat, M. ; Sauceau, M. ; Baillon, F. ; Le Barbenchon, L. ; Pedros, M. ; Dumon, M. Supercritical CO_2-assisted extrusion foaming: A suitable process to produce very lightweight acrylic polymer micro foams. *Journal of Applied Polymer* **2023**, *140* (3), e53277. DOI: 10.1002/app.53277

(53) Mae, H.; Omiya, M.; Kishimoto, K. Tensile behavior of polypropylene blended with bimodal distribution of styrene-ethylene-butadiene-styrene particle size. *Journal of Applied Polymer Science* **2008**, *107*, 3520–3528. DOI 10.1002/app.27482

(54) Svoboda, P.; Svobodova, D.; Slobodian, P.; Ougizawa, T.; Inoue, T. Transmission electron microscopy study of phase morphology in polypropylene/ethylene-octene copolymer blends. *European Polymer Journal* **2009**, *45*, 1485–1492. doi:10.1016/j.eurpolymj.2009.01.032

(55) Poelt, P.; Ingolic, E.; Gahleitner, M.; Bernreitner, K.; Geymayer, W. Characterization of modified polypropylene by scanning electron microscopy. *Journal of Applied Polymer Science* **2000**, *78*, 1152–1161. 10.1002/1097-4628(20001031)78:5<1152::AID-APP250>3.0.CO;2-7

(56) Hummel, R. A.; Moniot, R. Reconstructions from zero-crossings in scale space. *IEEE Transactions on Acoustics, Speech and Signal Processing* **1989**, *37* (12), 2111–2130. DOI: 10.1109/29.45555

(57) Alvarez, L.; Lions, P.-L.; Morel, J.-M. Image selective smoothing and edge detection by nonlinear diffusion. II. *SIAM Journal on Numerical Analysis* **1992**, *29* (3), 845–866. DOI: 10.1137/0729052

(58) Perona, P.; Malik, J. Scale space and edge detection using anisotropic diffusion. *Proceedings of the IEEE Computer Society Workshop on Computer Vision*, Miami; 1987, pages 16-22. ISBN: 0818607793

(59) Perona, P. ; Shiota, T. ; Malik, J. Anisotropic diffusion. In: *Geometry-Driven Diffusion in Computer Vision*. *Computational Imaging and Vision*, ter Haar Romeny, B. M., Eds.; vol 1. Springer, Dordrecht, pp 73–92, 1994. https://doi.org/10.1007/978-94-017-1699-4_3

(60) Deriche, R. ; Faugeras, O. *Les EDP en traitement des images et vision par ordinateur* ; Research Report 2697, INRIA, 1995. https://inria.hal.science/inria-00073993

(61) Grahs, T. Nonlinear anisotropic diffusion filters for the numerical approximation of conservation laws. Ph.D. Dissertation, Technischen Universität Braunschweig, 2002. https://doi.org/10.24355/dbbs.084-200511080100-585

(62) Krissian, K. ; Malandain, G. ; Ayache, N. *Directional anisotropic diffusion applied to segmentation of vessels in 3D images*; Research Report 3064, INRIA, 1996. https://inria.hal.science/inria-00073628

(63) Migeon, B.; Serfaty, V. *Filtrage EPSF pour l'amélioration d'image* ; Research Report 2175., INRIA, 1994. https://inria.hal.science/inria-00074498

(64) Tsiotsios, C.; Petrou, M. On the choice of the parameters for anisotropic diffusion in image processing. *Pattern Recognition* **2013**, *46* (5), 1369–1381. DOI: 10.1016/j.patcog.2012.11.012

(65) Canny, J. A computational approach to edge detection. *IEEE Transactions on Pattern Analysis and Machine Intelligence* **1986**, *PAMI-8* (6), 679–698. DOI: 10.1109/TPAMI.1986.4767851

(66) Gerig, G.; Kübler, O.; Kikinis, R.; Jolesz, F. A. Nonlinear anisotropic filtering of MRI data. *IEEE Transactions on Medical Imaging* **1992**, *11* (2), 221–232. DOI: 10.1109/42.141646

(67) Schulze M. A. Biomedical image processing with morphology-based nonlinear filters. Ph.D. Dissertation, University of Texas, Austin, 1994.

(68) Blanc-Féraud, L. ; Charbonnier, P. ; Aubert, G. ; Barlaud, M. Nonlinear image processing: modeling and fast algorithm for regularization with edge detection. *Proceedings of the IEEE International Conference on Image Processing*; 1995, Vol. 1, pp 474–477. https://doi.org/10.1109/ICIP.1995.529749

(69) Weeratunga, S. K.; Kamath, C. PDE-based nonlinear diffusion techniques for denoising scientific and industrial images: An empirical study. *Proceedings of the SPIE – The International Society for Optical Engineering;* 2002, Vol. 4667, pp 279–290. DOI: 10.1117/12.467989

(70) Acton, S. T. Multigrid anisotropic diffusion. *IEEE Transactions on Image Processing* **1998**, *7* (3), 280–291. DOI: 10.1109/83.661178

(71) Chao, S.-M.; Tsai, D.-M. Astronomical image restoration using an improved anisotropic diffusion. *Pattern Recognition Letters* **2006**, *27* (5), 335–344. DOI: 10.1016/j.patrec.2005.08.021

(72) Catté, F. ; Lions, P.-L. ; Morel, J.-M. ; Coll, T. Image selective smoothing and edge detection by nonlinear diffusion. *SIAM Journal on Numerical Analysis* **1992**, *29* (1), 182–193. DOI: 10.1137/0729012

(73) Nitzberg, M.; Shiota, T. Nonlinear image filtering with edge and corner enhancement. *IEEE Transactions on Pattern Analysis and Machine Intelligence* **1992**, *14* (8), 826–832. DOI: 10.1109/34.149593

(74) Niessen, W. J.; ter Haar Romery, B. M; Florack, L. M. J.; Salden, A. H.; Vergever, M. A. Nonlinear diffusion of scalar images using well-posed differential operators. *Proceedings of the IEEE Computer Society Conference on Computer Vision and Pattern Recognition;* 1994, pp 92–97. DOI: 10.1109/cvpr.1994.323815

(75) Weickert, J. A review of nonlinear diffusion filtering. In *Scale-Space Theory in Computer Vision. Scale-Space 1997*; ter Haar Romeny, B., Florack, L., Koenderink, J., Viergever, M. Eds.; Lecture Notes in Computer Science, vol 1252. Springer, Berlin, Heidelberg, 1997. https://doi.org/10.1007/3-540-63167-4_37

(76) Weickert, J. *Anisotropic diffusion in Image Processing*; ECMI Series, B.G. Teubner, Stuttgart, Germany, 1998.

(77) Weickert, J.; Benhamouda, B. A semi discrete nonlinear scale-space theory and its relation to the Perona-Malik paradox. In *Advances in Computer Vision. Advances in Computing Science*; Solina, F., Kropatsch, W. G., Klette, R., Bajcsy, R. Eds.; Springer, Vienna, 1997. https://doi.org/10.1007/978-3-7091-6867-7_1

(78) Chen, Y. ; Barcelos, C. A. Z. ; Mair, B. A. Smoothing and edge detection by time-varying coupled nonlinear diffusion equations. *Computer Vision and Image Understanding* **2001**, *82* (2), 85–100. DOI : 10.1006/cviu.2001.0903

(79) Morel, J.-M.; Solimini, S. *Variational Methods in Image Segmentation*; Birkhäuser Boston. 245 pages, 1995. ISBN: 0817637206, 9780817637200

(80) Nirenharg, L. A strong maximum principle for parabolic equations. *Communications on Pure and Applied Mathematics* **1953**, *VI*, 167–177. DOI: 10.1002/CPA.3160060202

(81) Green, P. J. Bayesian reconstruction from emission tomography data using a modified EM algorithm. *IEEE Transactions on Medical Imaging* **1990**, *9* (1), 84–93. DOI: 10.1109/42.52985

(82) Tschumperlé, D; Deriche, R. Anisotropic diffusion partial differential equations in multi-channel image processing: Framework and applications. In *Advances in Imaging and Electron Physics (AIEP*); Academic Press, pp 145–209, 2007. https://hal.science/hal-00332798

(83) Charbonnier, P. ; Blanc-Ferraud, L. ; Aubert, G. ; Barlaud, M. **1994**. Two deterministic half-quadratic regularization algorithms for computed imaging. *Proceedings of the International Conference on Image Processing*; 1995, Vol. 2*,* pp 168–172. DOI: 10.1109/ICIP.1994.413553

(84) Kapur, J. N.; Sahoo, P. K.; Wong, A. K. C. A new method for grey-level picture thresholding using the entropy of the histogram. *Computer Vision, Graphics, and Image Processing* **1985**, *29* (3), 273–285. DOI: 10.1016/0734-189X(85)90125-2

(85) Canseco, V.; Anguy, Y.; Roa, J. J.; Palomo, E. Structural and mechanical characterization of graphite foam / phase change material composites. *Carbon* **2014**, *74*, 266–281. http://dx.doi.org/10.1016/j.carbon.2014.03.031

(86) Vincent, L.; Dougherty, E. R. Morphological segmentation for textures and particles. In *Digital Image Processing Methods*; New York; Dougherty, E. R. Eds.; Marcel-Dekker, pp 43–102, 1994. http://dx.doi.org/10.1201/9781003067054-2

(87) Martinez-Marroquin, E. ; Jové, X ; de la Torre, F. ; Santamaria, E. Unsupervised morphological segmentation of objects in contact. *Proceedings of the 16ème Colloque Gretsi, Grenoble (France)*; 1997, pp 1379–1382. https://www.researchgate.net/publication/27608152_Unsupervised_morphological_segmentation_of_objects_in_contact

(88) Klette, R.; Rosenfeld, A. *Digital Geometry: Geometric Methods for Digital Picture Analysis*; Morgan Kaufman Publishers, 2004. ISBN: 9781558608610.

(89) Legland, D. ; Kiêu, K. ; Devaux, M.-F. Computation of Minkowski measures on 2D and 3D binary images. *Image Analysis and Stereology* **2007**, *26* (2), 83–92. DOI: 10.5566/ias.v26.p83-92

(90) Lehmann, G. G.; Legland, D. *Efficient N-dimensional surface estimation using Crofton formula and run-length encoding*; Research Report, 2012. https://hal.inrae.fr/hal-02811118

(91) Lang, C.; Ohser, J.; Hilfer, R. On the analysis of spatial binary images. *Journal of Microscopy* **2001**, *203* (3), 303–313. DOI: 10.1046/j.1365-2818.2001.00899.x

(92) Serra, J. *Image Analysis and Mathematical Morphology*; Vol. 1. London: Academic Press, 1982.

(93) Taki, K. Experimental and numerical studies on the effects of pressure release rate on number density of bubbles and bubble growth in a polymeric foaming process. *Chemical Engineering Science* **2008**, *63*, 3643–3653, doi: /10.1016/j.ces.2008.04.037

(94) Khan, I.; Costeux, S.; Adrian, D.; Bunker, S. Numerical studies of nucleation and bubble growth in thermoplastic foams at high nucleation rates. *Proceedings of the SPE Foams 2013 Conference*, Seattle, WA, United States, September 11–12, 2013. https://www.researchgate.net/publication/261172779_Numerical_Studies_of_Nucleation_and_Bubble_Growth_in_Thermoplastic_Foams_at_high_Nucleation_Rates

(95) Costeux, S. CO_2 blown nanocellular foams. *Journal of Applied Polymer Science* **2014**, 41293. DOI: 10.1002/app.41293

(96) Tammaro, D. ; Contaldi, V. ; Carbone, M. P. ; Di Maio, E. ; Iannace, S. A novel lab-scale batch foaming equipment: The mini-batch. *Journal of Cellular Plastics* **2016**, *52*, 533–543, doi: 10.1177/0021955X15584654

(97) McClurg, R. B. Design criteria for ideal foam nucleating agents. *Chemical Engineering Science* **2004**, *59* (24), 5779–5786. https://doi.org/10.1016/j.ces.2004.06.025

(98) Spitael, P.; Macosko, C. W.; McClurg, R. B. Block copolymer micelles for nucleation of microcellular thermoplastic foams, *Macromolecules* **2004**, *37* (18), 6874–6882. DOI: 10.1021/ma049712q

(99) Lee, M. S.; Lodge, T. P.; Macosko, C. W. Can Random Copolymers Serve as Effective Polymeric Compatibilizers? *Journal of Polymer Science: Part B: Polymer Physics* **1997**, *35* (17), 2835–2842. https://doi.org/10.1002/(SICI)1099-0488(199712)35:17<2835::AID-POLB8>3.0.CO;2-P

(100) Weickert, J.; Ter Haar Romeny, B. M.; Viergever, M. A. Efficient and reliable schemes for nonlinear diffusion filtering. *IEEE Transactions on Image Processing* **1998**, *7* (3), 398–410. DOI: 10.1109/83.661190

APPENDIX

NUMERICAL DISCRETIZATION

The nonlinear process in its form given in Eq. 4 was developed as

$$\partial_t u_{(\mathbf{x},t)} = \sum_i \partial_{x_i}\left(c_{(\mathbf{x},t)}\,\partial_{x_i} u_{(\mathbf{x},t)}\right) \qquad \text{Eq. 19}$$

This equation was discretized by finite differences by means of a simple explicit numerical scheme as

$$\frac{u_{(\mathbf{x},t+dt)} - u_{(\mathbf{x},t)}}{dt} \simeq \sum_i \frac{1}{dx_i}\partial_{x_i}\left(c_{(\mathbf{x},t)}\left(u_{\left(\mathbf{x}+\frac{dx_i}{2}\mathbf{e_i},\ t\right)} - u_{\left(\mathbf{x}-\frac{dx_i}{2}\mathbf{e_i},\ t\right)}\right)\right) \qquad \text{Eq. 20}$$

$$\begin{aligned}\frac{u_{(\mathbf{x},t+dt)} - u_{(\mathbf{x},t)}}{dt} = \sum_i \frac{1}{dx_i^2}\Bigg(& c_{\left(\mathbf{x}+\frac{dx_i}{2}\mathbf{e_i},\ t\right)}\left(u_{(\mathbf{x}+dx_i\,\mathbf{e_i},\ t)} - u_{(\mathbf{x},\ t)}\right)\cdots \\ & - c_{\left(\mathbf{x}-\frac{dx_i}{2}\mathbf{e_i},\ t\right)}\left(u_{(\mathbf{x},\ t)} - u_{(\mathbf{x}-dx_i\,\mathbf{e_i},\ t)}\right)\Bigg)\end{aligned} \qquad \text{Eq. 21}$$

where dx_i is the pixel size along the Cartesian direction i of unit vector $\mathbf{e_i}$.

In Eq. 21, the diffusion function $c(\|\nabla \mathrm{u}\|)$ is to be evaluated at points $\mathbf{x} \pm \frac{dx_i}{2}\,\mathbf{e_i}$ located at (the middle of) the boundary between two adjacent pixels. The diffusion being a function of the sole gradient of the intensity u, one could write

$$c(\|\nabla \mathrm{u}\|)_{\left(\mathbf{x}\pm\frac{dx_i}{2}\mathbf{e_i},\ t\right)} = c\left(\|\nabla \mathrm{u}\|_{\left(\mathbf{x}\pm\frac{dx_i}{2}\mathbf{e_i},\ t\right)}\right) \qquad \text{Eq. 22}$$

Therefore, a proper discretization of the gradient at the boundary between two pixels should be proposed. A gradient approximation by central differences gave

$$\|\nabla \mathrm{u}\|_{\left(\mathbf{x}\pm\frac{dx_i}{2}\mathbf{e_i},\ t\right)} = \sqrt{\sum_j \left(\partial_{x_j} u_{\left(\mathbf{x}\pm\frac{dx_i}{2}\mathbf{e_i},\ t\right)}\right)^2} = \sqrt{\sum_j \left(\frac{u_{\left(\mathbf{x}\pm\frac{dx_i}{2}\mathbf{e_i}+dx_j\mathbf{e_j},t\right)} - u_{\left(\mathbf{x}\pm\frac{dx_i}{2}\mathbf{e_i}-dx_j\mathbf{e_j},t\right)}}{2dx_j}\right)^2} \qquad \text{Eq. 23}$$

In the last term of this equation, the intensity u is to be evaluated at points $\mathbf{x} \pm \frac{dx_i}{2}\,\mathbf{e_i} + dx_j\mathbf{e_j}$ and $\mathbf{x} \pm \frac{dx_i}{2}\,\mathbf{e_i} - dx_j\mathbf{e_j}$ i.e., at the boundary between pairs of pixels. This was done by taking the average of the intensity u of the two adjacent pixels and the sought suitable discretization for the gradient $\|\nabla \mathrm{u}\|_{\left(\mathbf{x}\pm\frac{dx_i}{2}\mathbf{e_i},\ t\right)}$ at the boundary between two pixels reads

$$\|\nabla \mathrm{u}\|_{\left(\mathbf{x}\pm\frac{dx_i}{2}\mathbf{e_i},t\right)} = \sqrt{\sum_j \frac{1}{4dx_j}\left(u_{(\mathbf{x}\pm dx_i\,\mathbf{e_i}+dx_j\mathbf{e_j},t)} + u_{(\mathbf{x}+dx_j\mathbf{e_j},t)} - u_{(\mathbf{x}\pm dx_i\,\mathbf{e_i}-dx_j\mathbf{e_j},t)} - u_{(\mathbf{x}-dx_j\mathbf{e_j},t)}\right)^2} \qquad \text{Eq. 24}$$

This expression remains valid at the boundary pixels as the image is extended by reflecting it at the boundary [100].